ADVANCED SCIENCE Open Access
www.advancedscience.com

Extracellular Matrix Sulfation in the Tumor Microenvironment Stimulates Cancer Stemness and Invasiveness

*Alican Kuşoğlu, Deniz Örnek, Aslı Dansık, Ceren Uzun, Sena Nur Özkan, Sevgi Sarıca, Kardelen Yangın, Şevval Özdinç, Duygu Turan Sorhun, Nuriye Solcan, Efe Can Doğanalp, Øystein Arlov, Katherine Cunningham, Ismail C. Karaoğlu, Seda Kizilel, Ihsan Solaroğlu, Pınar Bulutay, Pınar Fırat, Suat Erus, Serhan Tanju, Şükrü Dilege, Gordana Vunjak-Novakovic, Nurcan Tuncbag, and Ece Öztürk**

Tumor extracellular matrices (ECM) exhibit aberrant changes in composition and mechanics compared to normal tissues. Proteoglycans (PG) are vital regulators of cellular signaling in the ECM with the ability to modulate receptor tyrosine kinase (RTK) activation via their sulfated glycosaminoglycan (sGAG) side chains. However, their role on tumor cell behavior is controversial. Here, it is demonstrated that PGs are heavily expressed in lung adenocarcinoma (LUAD) patients in correlation with invasive phenotype and poor prognosis. A bioengineered human lung tumor model that recapitulates the increase of sGAGs in tumors in an organotypic matrix with independent control of stiffness, viscoelasticity, ligand density, and porosity, is developed. This model reveals that increased sulfation stimulates extensive proliferation, epithelial-mesenchymal transition (EMT), and stemness in cancer cells. The focal adhesion kinase (FAK)-phosphatidylinositol 3-kinase (PI3K) signaling axis is identified as a mediator of sulfation-induced molecular changes in cells upon activation of a distinct set of RTKs within tumor-mimetic hydrogels. The study shows that the transcriptomic landscape of tumor cells in response to increased sulfation resembles native PG-rich patient tumors by employing integrative omics and network modeling approaches.

1. Introduction

The tumor microenvironment (TME) is a dynamic niche in which tumor cells and a plethora of stromal and immune cell types interact within tumor-specific extracellular matrix (ECM), and plays a fundamental role in regulating signaling events involved in tumorigenesis and dissemination.[1] The biochemical and mechanical characteristics of ECM are deregulated during malignancy, resulting in activation of various cellular mechanisms that partake in tumor growth, angiogenesis, metastasis, and immune suppression.[2] Dissecting the effect of aberrant changes in the ECM on tumor cell behavior is crucial for a deeper understanding of the complex orchestration of signaling events that govern disease progression. This calls for human tumor models with the ability to recapitulate the key aspects of the ECM and enable their controlled tunability. The need for such models

A. Kuşoğlu, D. Örnek, A. Dansık, S. Nur Özkan, S. Sarıca, K. Yangın, Ş. Özdinç, D. T. Sorhun, N. Solcan, E. C. Doğanalp, E. Öztürk
Engineered Cancer and Organ Models Laboratory
Koç University
Istanbul 34450, Turkey
E-mail: ozturkece@ku.edu.tr

The ORCID identification number(s) for the author(s) of this article can be found under https://doi.org/10.1002/advs.202309966

DOI: 10.1002/advs.202309966

A. Kuşoğlu, D. Örnek, A. Dansık, S. Nur Özkan, S. Sarıca, K. Yangın, Ş. Özdinç, D. T. Sorhun, E. C. Doğanalp, S. Kizilel, I. Solaroğlu, N. Tuncbag, E. Öztürk
Research Center for Translational Medicine (KUTTAM)
Koç University
Istanbul 34450, Turkey

A. Kuşoğlu, D. Örnek, S. Nur Özkan, S. Sarıca, K. Yangın, Ş. Özdinç, D. T. Sorhun
Graduate School of Health Sciences
Koç University
Istanbul 34450, Turkey

A. Dansık, C. Uzun, N. Solcan
Graduate School of Sciences and Engineering
Koç University
Istanbul 34450, Turkey

has led to an intersection of tissue engineering and cancer research. Biological materials such as reconstituted basement membrane (rBM) and collagen as well as synthetic polymers such as polyethylene glycol (PEG) have become gold standard tools for 3D in vitro modeling of tumor tissues that established the importance of replicating tumor mechanics and composition.[3–5]

Tumors are marked by distinct expression of cell instructive ECM ligands compared to native organs where they emerge.[6] Proteoglycans (PGs) are heterogenous glycoproteins with sulfated glycosaminoglycan (sGAG) side chains that have vital functions in the ECM.[7] Due to their negatively charged sulfate moieties, sGAGs infer affinity to bioactive ligands, control their availability and mediate formation of ternary complexes with ligands and receptor tyrosine kinases (RTKs) which lead to their activation and downstream signaling cascades.[7] RTK family receptor signaling has key roles in many stages of tumor progression and most cancers are characterized with driver mutations in RTKs.[8] Expectedly, many types of tumor tissues demonstrate increase in sGAG content and altered sulfation pattern.[9] Although deregulation of sGAG biosynthesis and post-translational modification have been shown to correlate with poor prognosis, the effect of the increase in sGAGs on tumor growth and invasion has been controversial.[9,10] Studies have reported both tumor promoting and inhibiting effects of sGAG supplementation.[10c,11] The use of sGAGs has even been proposed as a therapeutic approach in cancer.[12] These studies strongly suggest the need for an unprecedented 3D human tumor model with ability to present sGAGs to tumor cells within their microenvironmental milieu and allow recapitulation of their aberrant increase while having control over ECM content, stiffness, viscoelasticity, and network porosity to elucidate their distinct effects on tumor cells.

To investigate the effect of increased sulfation within an engineered model, a representation of the heathy tissue ECM onto which malignant characteristics could be controllably introduced is required. However, materials such as rBM, which is derived from Engelbreth-Holm-Swarm (EHS) sarcoma and has an undefined composition with high variability, lack a faithful recapitulation of healthy ECM.[3] Decellularization of native organs offers the advantage of preserving the tissue-specific composition of ECM.[13] We have recently developed bovine-derived decellularized lung ECM hydrogels with low batch-to-batch variability and high compositional resemblance to human lungs.[14] On the other hand, the use of native sGAGs as well as sGAG-mimetic materials has been pursued in tissue engineering.[5a,15] Alginate, an inert biopolymer, can be sulfated to successfully mimic native sGAGs in both exerting affinity to growth factors and mediating their interactions with RTKs.[15] Precise tunability of sulfation and enabling of the alginate backbone for mechanical modulation renders this approach advantageous over the use of native sGAGs.

Here, we introduce a biomaterial-based 3D human lung tumor model constituted of double-network hydrogels of decellularized lung ECM with sGAG-mimetic alginate sulfate to investigate the effect of sulfation in the TME on the growth and progression of lung tumor cells. Addressing the aforementioned challenges, our model allows tunability of sulfation within an organotypic network while enabling control over ligand density and tissue mechanics. Our data demonstrates that increased sulfation acts as an essential regulator in the lung TME which promotes growth, stemness and epithelial-mesenchymal transition (EMT) via the RTK-phosphatidylinositol 3-kinase (PI3K) signaling axis.

2. Results

2.1. Elevated PG Expression Correlates with Invasiveness and Poor Survival in Lung Adenocarcinoma (LUAD) Patients

Non-small cell LUAD is the most common type of lung cancer, the leading cause of cancer-related mortality worldwide.[16] To validate our hypothesis of sulfation-mediated regulation of tumor progression, we initially performed bioinformatics analyses on a 510-patient LUAD cohort to reveal differential expression of PGs in patient tumors. Analyses of RNA sequencing (RNAseq) data derived from The Cancer Genome Atlas (TCGA) for 34 PG-encoding genes in LUAD samples relative to normal lung tissue demonstrated that the expression of the majority of PG genes was increased in patient tumors (**Figure 1a**). We then defined two patient groups within the cohort. PG positive (PG+) group included patients which had z-score equal to or higher than a cut-off value of three for at least three PG genes, whereas PG negative (PG-) group had zero genes. PG+ group represented 48% of all patients, had more than fivefold higher number of patients, significantly higher PG score and a poorer survival curve compared to the PG- group (Figure 1b–d). EMT in lung cancer cells highly correlates with poor prognosis.[17] We next calculated the EMT and invasiveness scores for all patients from the RNAseq data (see Experimental Section). The correlation of both scores with the PG scores of LUAD patients was strikingly

Ø. Arlov
Department of Biotechnology and Nanomedicine
SINTEF Industry
Trondheim 7034, Norway
K. Cunningham, G. Vunjak-Novakovic
Department of Biomedical Engineering
Columbia University
New York, NY 10027, USA
I. C. Karaoğlu, S. Kizilel, N. Tuncbag
Chemical and Biological Engineering
Koç University
Istanbul 34450, Turkey
I. Solaroğlu
Department of Neurosurgery
School of Medicine
Koç University
Istanbul 34450, Turkey
P. Bulutay, P. Fırat
Department of Pathology
School of Medicine
Koç University
Istanbul 34450, Turkey
S. Erus, S. Tanju, Ş. Dilege
Department of Thoracic Surgery
School of Medicine
Koç University
Istanbul 34450, Turkey
N. Tuncbag, E. Öztürk
Department of Medical Biology
School of Medicine
Koç University
Istanbul 34450, Turkey

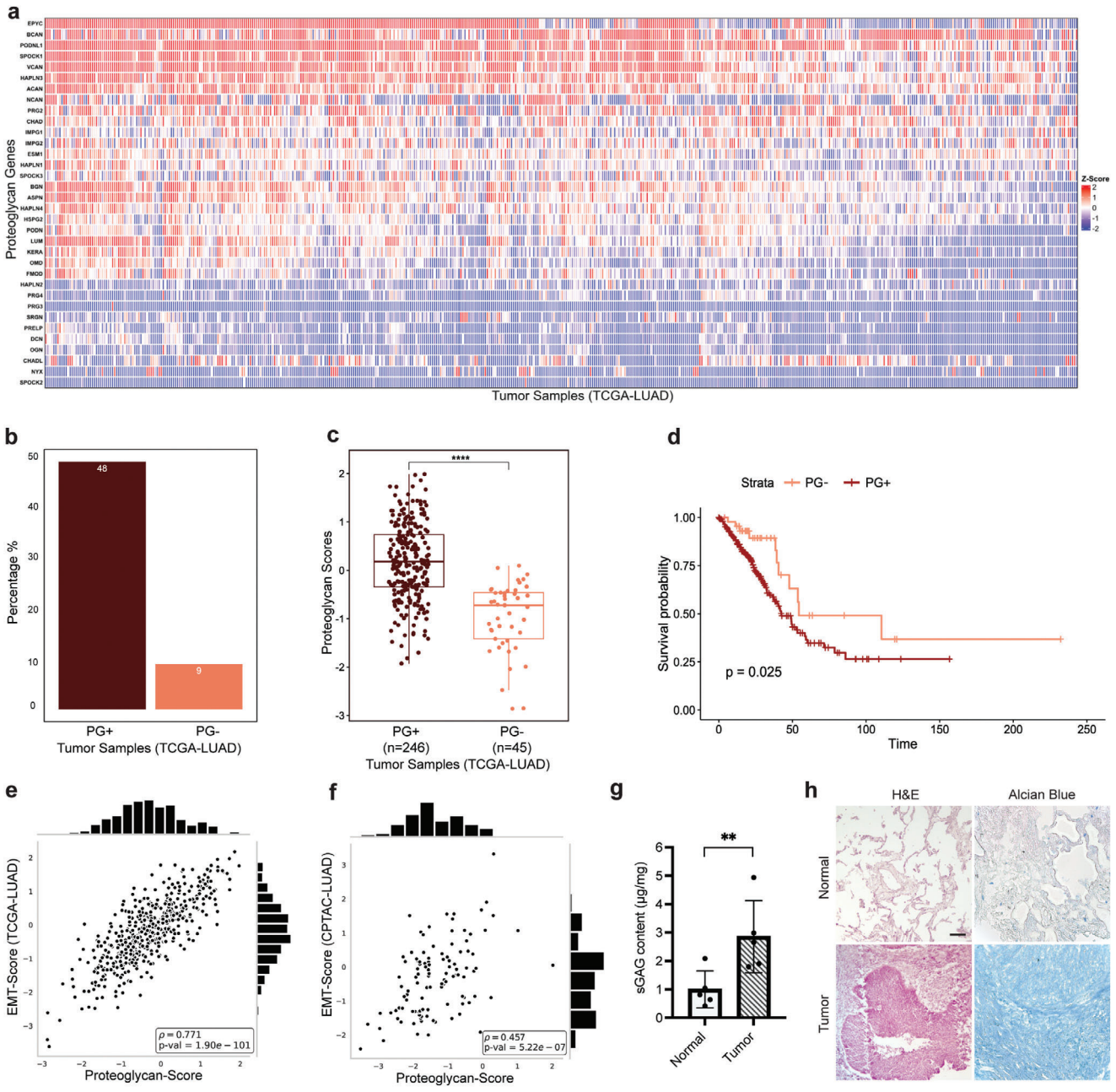

Figure 1. Elevated PG expression correlates with invasiveness and poor survival in LUAD patients. a) Hierarchical clustering heatmap of PG mRNA expression z-scores in LUAD patient tumors relative to normal tissue samples where the rows represent PG genes and columns indicate patients. b) Percentages of PG+ and PG- tumor samples in TCGA LUAD patient cohort. A sample is considered PG+ if z-score is greater than the cut-off of three for at least three genes, while a sample is considered PG- if the z-score is higher than the cut-off, but the number of genes is equal to zero. c) Box plot comparison of PG scores of PG+ and PG- patient groups. Each box extends from the lower to the upper quartile where the horizontal line indicates the median value. Each dot represents the PG score of an individual patient. Statistical analysis was performed with Wilcoxon test, $p = 1.5e^{-14}$. d) Survival plots of PG+ and PG- LUAD patients. Log-rank test was used to assess significance, $p = 0.025$. e) Regression analysis on EMT scores and PG scores using the mRNA ($p = 1.9e^{-101}$) and f) protein expressions ($p = 5.22e^{-07}$). Spearman rank correlation was used to calculate the correlation values (ρ). g) sGAG quantification in LUAD patient-derived tumor and matched normal lung samples, n = 5 biological replicates. Data is represented as mean ± S.D and statistical significance was analyzed using a paired, two-tailed student's *t*-test, $p < 0.01$. h) Hematoxylin and eosin (H&E) and Alcian blue staining of normal lung parenchyma and tumor tissue (scale bar: 100 µm).

high (ρ = 0.771 for EMT, ρ = 0.86 for invasiveness) (Figure 1e; Figure S1, Supporting Information). EMT and PG scores of patients were also calculated for protein expression from Clinical Proteomic Tumor Analysis Consortium (CPTAC) data which similarly showed a significantly high correlation (ρ = 0.457) (Figure 1f).[18] We then collected surgically resected tumor and matched healthy parenchyma tissues from 5 LUAD patients to perform sGAG quantification and histopathological assessments. Patient-derived tumor tissues had significantly higher amounts of sGAGs (2.85-fold) than normal tissues (Figure 1g). Consistently, Alcian blue staining revealed increased sGAG deposition in tumor tissues (Figure 1h). Together, these results confirmed the relevance of biomimicking the increased sulfation of lung tumor matrices with an engineered human tumor model.

2.2. Mimicking the Increased Sulfation in the TME Drives Aberrant Proliferation of Lung Tumor Cells

To model the increase of sulfation in the TME, decellularized and reconstituted lung-derived ECM (dLung), representing the matrix composition at the tumor's site of origin, was combined with either alginate (Alg) or sGAG-mimetic alginate sulfate (S-Alg) to obtain interpenetrating, double-network hydrogels (**Figure 2**a). Decellularization of bovine lungs was carried out following our freeze-thaw method and validated for elimination of nuclear content, preservation of ECM constituents, gelation, and biocompatibility (Figure 2a; Figure S2, Supporting Information).[14] Degree of sulfation (DS) of alginate can be tuned without altering structural features of the polymer such as monosaccharide structure, chain confirmation, and flexibility.[15b] Sulfation of alginate was performed to yield a DS value of 0.41 sulfate groups per monomer (Figure S3, Supporting Information). Tumor-mimetic hydrogels were fabricated with dLung and S-Alg, S-AlgLung, whereas healthy-mimetic hydrogels, AlgLung, comprised of unmodified alginate. Both hydrogels had equal concentration of dLung (5,4 mg mL^{-1}) and alginates (10 mg mL^{-1}). Alginate and derivatives, due to their ionic crosslinking capability in the presence of divalent cations allow tunability of stiffness independently from ECM composition and porosity.[19] We modulated crosslinker (Ca^{2+}) density to match the stiffness of the tumor-mimetic (S-AlgLung) and healthy-mimetic (AlgLung) hydrogels which demonstrated similar storage moduli and loss tangent with oscillatory rheology (Figure 2b,c; Figure S4, Supporting Information). The stiffness range for the hydrogels was tuned to match the stiffness of healthy lung tissue, whose Young's modulus was reported in 1–2 kPa range.[20] This was aimed to investigate the sole effect of increased sulfation in the TME without the effect of stiffening. PGs have been shown to interact with mechanosensitive receptors such as integrin family to induce distinct synergistic signaling pathways.[21] Apart from stiffness, viscoelasticity has been shown to be an important parameter that affects cancer cell behavior. Modulation of molecular weight has been reported as a means to tune plasticity of alginate hydrogels.[22] Sulfation caused a significant decrease in the molecular weight of alginate as indicated by size exclusion chromatography without compromising its hydrogel forming capacity (Figure 2d, Table S1, Supporting Information). Therefore, we investigated the stress-relaxation behavior of AlgLung and S-AlgLung hydrogels with a creep-recovery test. Surprisingly, the two hydrogels demonstrated very similar relaxation curves and permanent strain values (Figure 2e,f). Next, we assessed porosity in the hydrogels with dextran release assay using two different sizes (10 kDa and 70 kDa) which showed similar release curves for both AlgLung and S-AlgLung (Figure 2g,h). Thus, our model allowed alteration of sulfation in the presence of organotypic ECM independently from ligand density, hydrogel stiffness, plasticity, and porosity.

To investigate the effects of increased sulfation on cellular proliferation, we encapsulated LUAD-derived A549 cells into AlgLung and S-AlgLung hydrogels and cultured up to 4 weeks. S-AlgLung hydrogels stimulated extensive growth of A549 cells starting from the first week (Figure 2i,j). Ki67 staining further validated the increased proliferation of tumor cells in S-AlgLung hydrogels (Figure S5, Supporting Information). Cell viability was not compromised with unmodified alginate in AlgLung hydrogels but rather cell growth was limited (Figure S6, Supporting Information). Moreover, when cells were cultured in double-network hydrogels of alginate and rBM (Matrigel), AlgMat, potent cell growth was again observed demonstrating the growth-limiting effect of organotypic lung matrix (Figure S7, Supporting Information). AlgMat hydrogels had over twofold higher amount of sGAGs than AlgLung (Figure S8, Supporting Information), however, the undefined, tumor-derived composition of Matrigel does not allow the attribution of observed phenomena to a single component. This further emphasizes the advantage of using healthy tissue-derived matrices and introduction of malignant ECM parameters in a controllable fashion to model their effects on cancer cells. Cellular clump formation in hydrogels was analyzed which exhibited a significant increase in clump number and area in S-AlgLung hydrogels as well as a decrease in clump circularity indicating a more invasive phenotype (Figure 2k,l,m). In line with invasiveness, collective cell migration was observed at the periphery of S-AlgLung hydrogels at week 4, suggesting that the sulfated microenvironment both promoted clump formation and facilitated migration (Figure S9, Supporting Information). For quantification of cell migration, a transwell membrane-based assay was utilized which confirmed a significant increase in the number of cells migrating from S-AlgLung hydrogels (Figure S10, Supporting Information). We next stained cells with histopathological markers for non-small cell lung cancer (NSCLC), thyroid transcription factor (TTF-1), and tumor protein p63 (Figure 2n).[23] Cells in S-AlgLung hydrogels stained positive for TTF-1, a common lineage marker for diagnosis, which is significantly increased in lung tumors compared to normal tissue.[24] p63, a characteristic marker for squamous carcinoma, is found in a subset of adenocarcinomas and is a potent regulator of proliferation and cluster formation.[25] Recently, TTF-1/p63 double-positive LUAD tumors have been dubbed as a basal-like and aggressive phenotype in line with the proliferative and invasive phenotype we observe in S-AlgLung hydrogels.[26]

2.3. Increased Sulfation in the ECM Modulates EMT and Cancer Stemness

sGAGs regulate RTK signaling which in turn activates signaling routes that promote EMT, tumor cell motility and metastasis.[8,9]

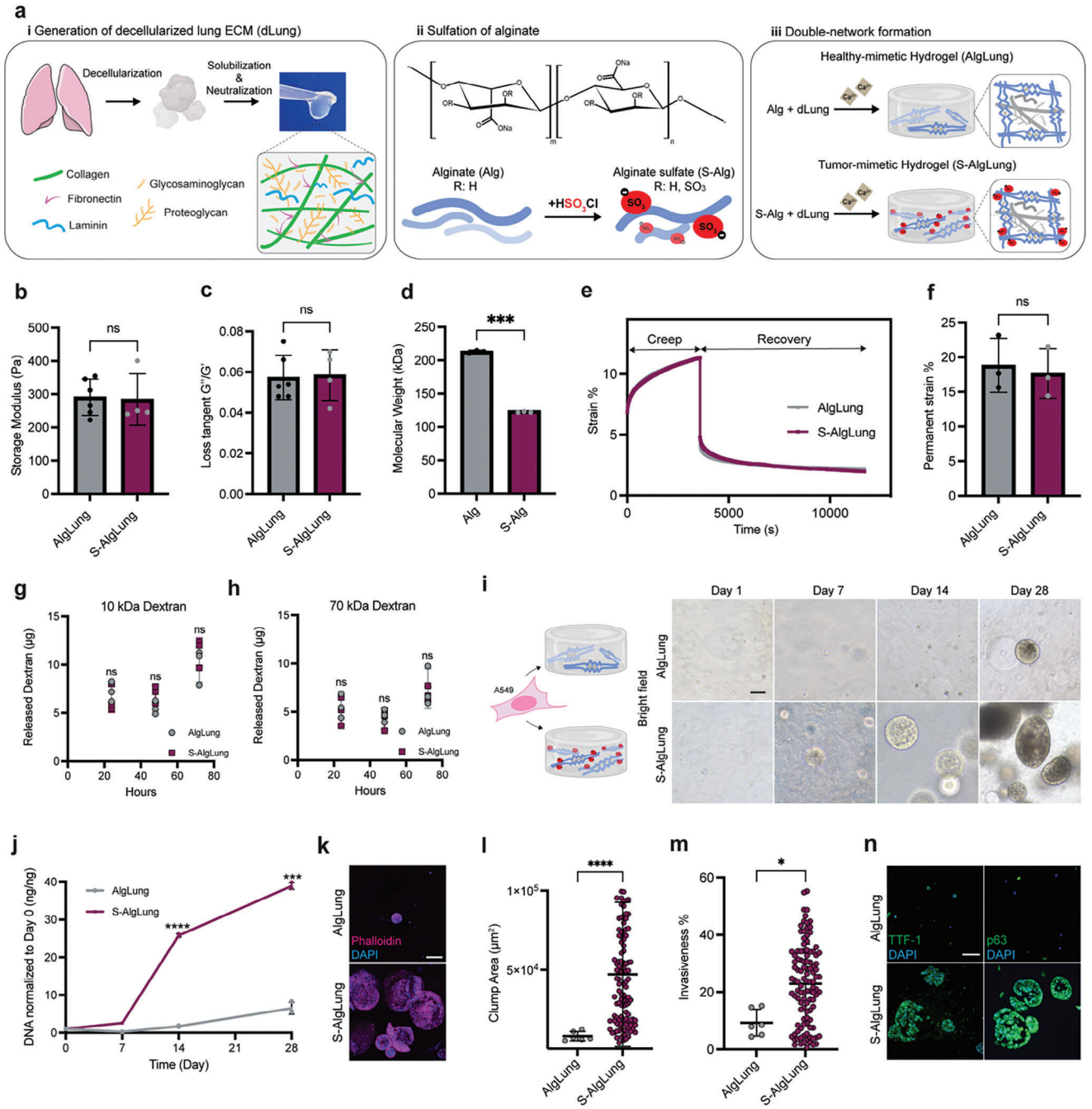

Figure 2. Mimicking the increased sulfation in the TME drives aberrant proliferation of lung tumor cells. a) Schematic illustration of the fabrication of AlgLung and S-AlgLung hydrogels using decellularized lung ECM and alginate/alginate sulfate. b) Storage modulus and c) Loss tangent (G″/G′) of AlgLung and S-AlgLung hydrogels, ns not significant. d) Molecular weight of alginate (Alg) and alginate sulfate (S-Alg) characterized by SEC-MALS, $p < 0.001$. e) Creep and Recovery test of AlgLung and S-AlgLung hydrogels. f) Permanent strain of AlgLung and S-AlgLung hydrogels obtained from creep and recovery tests, ns not significant. g) 10 kDa and h) 70 kDa dextran release from AlgLung and S-AlgLung hydrogels over 72 h, ns not significant. i) Bright field images of A549 cells in AlgLung and S-AlgLung hydrogels at day 1, 7, 14, and 28. j) Quantification of DNA content in AlgLung and S-AlgLung hydrogels normalized to day 0, $^{**}p < 0.01$, $^{***}p < 0.001$. k) Immunofluorescence image of A549 clusters stained for Phalloidin (magenta) and DAPI (blue) in AlgLung and S-AlgLung hydrogels (scale bar: 100 μm). l) Quantification of cluster area (μm^2) and m) invasiveness (%) of cells grown in AlgLung and S-AlgLung hydrogels at day 28, $^{*}p < 0.05$, $^{****}p < 0.0001$. n) Immunofluorescence staining of LUAD markers TTF-1 and p63 (green) and DAPI (blue) in A549 cells grown in AlgLung and S-AlgLung hydrogels (scale bar: 100 μm). Quantitative data is represented as mean ± S.D, and statistical significance was analyzed using an unpaired, two-tailed student's *t*-test.

Therefore, we explored the EMT process that might induce an invasive phenotype in sulfated hydrogels. Immunofluorescence staining revealed elevated expression of mesenchymal markers including N-cadherin, vimentin, and fibronectin in S-AlgLung hydrogels (**Figure 3a**). Consistently, expression of CDH2 (N-cadherin), vimentin and FN1 (fibronectin) genes were significantly increased in sulfated hydrogels (Figure 3b). In contrast, we observed an upregulation of epithelial marker E-cadherin on both protein (Figure 3a) and gene (CDH1) (Figure 3b) levels in sulfated hydrogels, indicating a lack of conventional "cadherin-switch" but a more dynamic transition between epithelial-mesenchymal states normally observed in metastatic tumor cells.[27,28] Besides, E-cadherin is a promoter of spheroid formation correlating with the increased number of clusters in sulfated hydrogels which exhibit localization of E-cadherin in the periphery (Figure 3a). Gene expression of epithelial markers EPCAM and ZO-1 (TJP1) were similarly significantly upregulated in S-AlgLung hydrogels. However, ZO-1 protein expression was observed to be prominent in the periphery of cellular clumps in AlgLung hydrogels suggesting a tighter epithelial barrier (Figure S11, Supporting Information).[29] Such complex, co-expression of epithelial and mesenchymal markers is not atypical for clinical LUAD samples that was recapitulated in tumor-mimetic hydrogels.[30] Moreover, sulfated hydrogels strongly induced the expression of several EMT-regulating transcription factors such as ZEB1, ZEB2, and SNAIL (Figure 3b), further emphasizing the role of ECM sulfation (Figure 3c).

Recent studies suggest that secretory mucins MUC5AC and MUC5B are aberrantly expressed in tumor tissues and associated with distant metastases and poor survival in LUAD patients.[31] MUC5B staining reveals enhanced deposition in S-AlgLung hydrogels (Figure 3d) in line with significantly increased expression of MUC5AC and MUC5B genes (Figure 3e). Interestingly, studies showed that activation of EMT process can increase cancer stem cell (CSC) population with self-renewal capacity within tumors.[32] Furthermore, a correlation between CSC phenotype and the expression of several mucins have been reported.[33] Thus, we next investigated whether sulfated ECM could stimulate stemness in cancer cells. Expression of SOX2, an important stemness marker and regulator of EMT program, was potently increased in S-AlgLung hydrogels (Figure 3f). Similarly, gene expression of stemness markers SOX2, KLF4, OCT3/4, CD44, and CD133 exhibited strong upregulation upon sulfation (Figure 3g). sGAGs have been proposed to have a role in regulation of stemness through modulation of WNT/beta-catenin pathway.[34] Consistently, beta-catenin also demonstrated higher expression in sulfated hydrogels (Figure 3f). Next, we encapsulated pre-formed spheroids within AlgLung and S-AlgLung hydrogels to provide functional insights on the sulfation-induced stemness of A549 cells. Spheroids in S-AlgLung hydrogels demonstrated extensive growth, significantly higher spheroid area and invasiveness compared to AlgLung (Figure 3h,i; Figure S12, Supporting Information), further showing that sulfated ECM supports phenotypes typically observed in CSCs as metastasis initiators.[35] We then investigated the correlation of PG expression and stemness (CSC-score) in the TCGA LUAD cohort which revealed a significant correlation (ρ = 0.457) (Figure 3j). Overall, these findings further validate that increased sulfation in lung tumors promotes an aggressive, mucinous and stem-like phenotype.

2.4. RTK Signaling Mediates Sulfation-Induced Tumorigenic Phenotype

Next, we wanted to uncover the molecular pathways mediating the response of lung tumor cells to sulfated ECM. sGAGs modulate the common RTK pathways through both increased retention of ligands and enabling ligand-receptor complexes that leads to receptor activation.[7] Epidermal growth factor receptor (EGFR) is overexpressed in more than 25% of LUAD cases which correlates with poor prognosis. Integrin β1 was suggested to be required for the ligand-mediated activation of EGFR.[36] We thus examined EGFR and integrin β1 expression of lung tumor cells in AlgLung and S-AlgLung hydrogels. Both receptors were positively stained on the cell membrane of A549 cells in S-AlgLung hydrogels (**Figure 4a**). However, inhibition of neither receptor was able to block sulfation-induced tumor cell growth in sulfated gels (Figure 4b,c). We then blocked other RTKs including fibroblast growth factor receptor (FGFR) and transforming growth factor β receptor (TGFβR). Blocking only FGFR and TGFβR resulted in inhibition of cell growth in S-AlgLung hydrogels. Moreover, further blocking EGFR, FGFR, and TGFβR together enhanced the inhibitory effect of TGFβR alone but not FGFR (Figure 4d,e). Next, we performed a phospho-RTK array (49 human RTKs) to validate the phosphorylation of FGFR and screened for other possible RTKs that might be activated upon interaction with sulfated ECM (Figure 4f). Phosphorylation of FGFR3, a RTK recently reported to be highly expressed in NSCLC samples[37] but not FGFR1 was induced in S-AlgLung hydrogels (Figure S13, Supporting Information). Interestingly, phosphorylated EGFR was even reduced in sulfated gels (Figure S13, Supporting Information). Phosphorylation of RYK, a receptor with a regulatory role in canonical and non-canonical Wnt signaling,[38] was also induced in S-AlgLung in line with expression of beta-catenin and upregulation of Wnt-5a ligand (Figure 3f; Figure S14, Supporting Information).

We further validated the sulfation-induced activation of the FGFR3 receptor with Western blotting which revealed an increased ratio of pFGFR3/total FGFR3 in S-AlgLung hydrogels (Figure S15, Supporting Information). To further elaborate on the functional role of FGFR3 activation on sulfation-induced lung tumor cell growth, we selectively inhibited the activation of FGFR3 by administering clinically used monoclonal antibody, Vofatamab (B-701).[39] Selective inhibition of FGFR3 significantly decreased the proliferation capacity as well as clump area of A549 cells encapsulated in S-AlgLung hydrogels (Figure 4g,h; Figure S16, Supporting Information). Therefore, we have established that the phosphorylation of FGFR3 is required to maintain the sulfation-induced tumorigenicity of A549 cells. After confirming the distinct phosphorylated RTKs in sulfated ECM, we next sought to elucidate the downstream signaling route that controls the sulfation-induced effects. We treated A549 cells in S-AlgLung hydrogels with small molecule inhibitors targeting the PI3K-Akt-mTOR, CDC42-NWASP-Arp2/3 as well as focal adhesion kinase (FAK) signaling axes. Inhibition of PI3K, mTOR as well as FAK

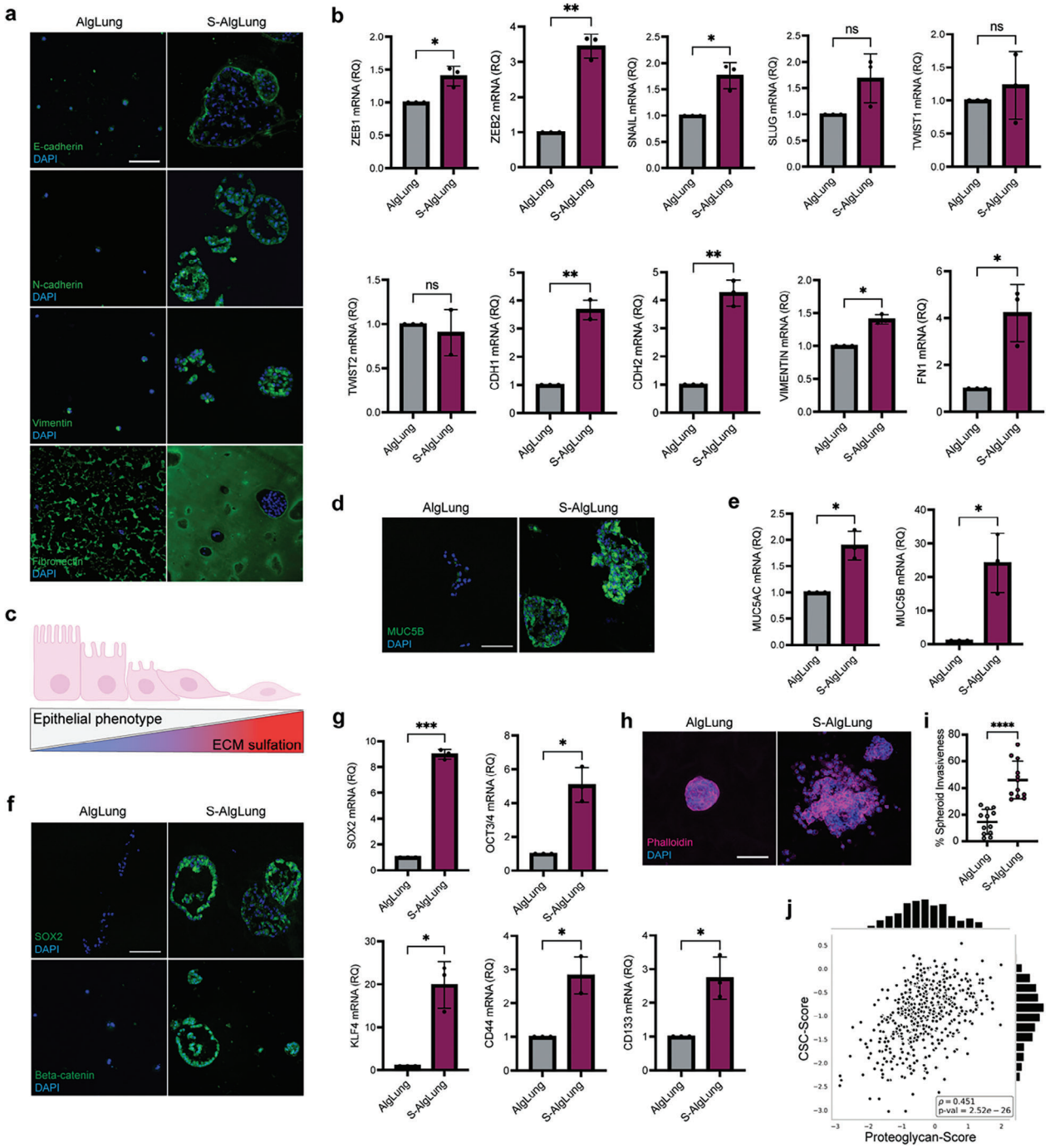

Figure 3. Increased sulfation in the ECM modulates EMT and cancer stemness. a) Immunofluorescence staining for E-cadherin, N-cadherin, vimentin and fibronectin (green, top to bottom) and DAPI (blue) in A549 cells grown AlgLung and S-AlgLung hydrogels (scale bar = 100 µm). b) mRNA expression of EMT regulators and markers in A549 cells grown in AlgLung and S-AlgLung hydrogels, ns not significant, $*p < 0.05$, $*p < 0.01$. c) Schematic illustration showing the inverse correlation between epithelial phenotype and ECM sulfation. d) Immunofluorescence staining of MUC5B (green) and DAPI (blue) in A549 cells grown in AlgLung and S-AlgLung hydrogels (scale bar: 100 µm). e) mRNA expression of MUC5AC and MUC5B in A549 cells grown in AlgLung and S-AlgLung hydrogels, $*p < 0.05$. f) Immunofluorescence staining of SOX2 (top) and beta-catenin (bottom) (green) and DAPI (blue) in A549 cells grown in AlgLung and S-AlgLung hydrogels (scale bar: 100 µm). g) mRNA expression of stemness markers in A549 cells grown in AlgLung and S-AlgLung hydrogels, $*p < 0.05$, $***p < 0.001$. h) Immunofluorescence image of A549 spheroids stained for Phalloidin (magenta) and DAPI (blue) in AlgLung and S-AlgLung hydrogels (scale bar: 100 µm). i) Quantification of cluster invasiveness (%) of spheroids grown in AlgLung and S-AlgLung hydrogels at day 21, $*p < 0.0001$. j) Regression analysis of cancer stem cell (CSC) genes and PGs using the mRNA expression scores in TCGA LUAD patient cohort. Spearman rank correlation was used to calculate the correlation values (ρ) ($p = 2.52e^{-26}$). b,e,g) Relative quantification (RQ) was used with normalization to AlgLung samples. Data is represented as mean ± S.D and statistical significance was analyzed using an unpaired, two-tailed student's *t*-test.

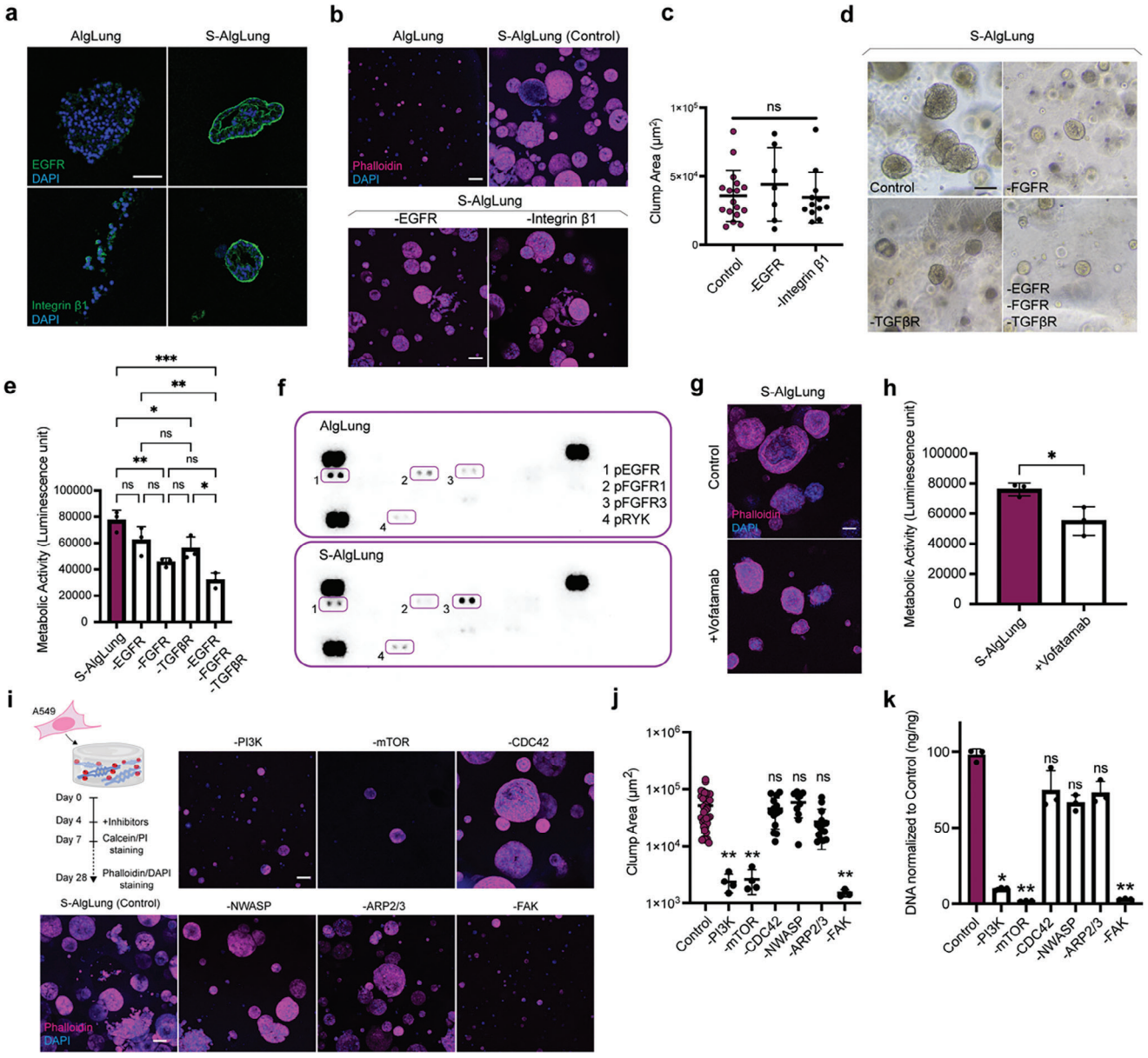

Figure 4. RTK signaling mediates sulfation-induced tumorigenic phenotype. a) Immunofluorescence staining of EGFR (top) and integrin β1 (bottom) (green) and DAPI (blue) in A549 cells grown in AlgLung and S-AlgLung hydrogels (scale bar: 100 μm). b) Representative images of phalloidin (magenta) and DAPI (blue) stained A549 cells in AlgLung and S-AlgLung hydrogels treated with EGFR and integrin β1 inhibitors (scale bar: 100 μm). c) Quantification of cluster area (μm^2) of A549 cells in S-AlgLung hydrogels treated with EGFR and integrin β1 inhibitors, ns not significant. d) Representative brightfield images of A549 cells grown in S-AlgLung and treated with RTK inhibitors at day 14, (scale bar: 100 μm). e) Metabolic activity analysis of A549 cells in S-AlgLung hydrogels and treated with RTK inhibitors. Values were normalized to control group, ns not significant, *$p < 0.05$, **$p < 0.01$, ***$p < 0.001$. f) Human Phospho-RTK Array performed on A549 cells grown in AlgLung and S-AlgLung hydrogels for 21 days. RTKs were framed up and footnoted. g) Representative images of phalloidin (magenta) and DAPI (blue) stained A549 cells in S-AlgLung hydrogels treated with vofatamab (scale bar: 100 μm). h) Metabolic activity analysis of A549 cells in S-AlgLung and vofatamab treated hydrogels using CellTiter-Glo 3D assay, *$p < 0.05$. i) Representative images of phalloidin (magenta) and DAPI (blue) stained A549 cells S-AlgLung hydrogels treated with indicated inhibitors (scale bar: 100 μm). j) Quantification of cluster area (μm^2) of A549 cells in S-AlgLung hydrogels treated with indicated inhibitors, ns not significant, **$p < 0.01$. k) Quantification of DNA content of A549 cells grown in S-AlgLung hydrogels and treated with indicated inhibitors. Values were normalized to control group, ns not significant, *$p < 0.05$, **$p < 0.01$. Quantitative data is represented as mean ± S.D and statistical significance was analyzed using ordinary one-way Anova analysis.

completely abrogated the sulfation effect on cell growth without compromising viability (Figure 4i–k) (Figure S17, Supporting Information).

2.5. PI3K is a Key Regulator of Sulfation-Induced Tumorigenic Phenotype

Next, we focused on PI3K since it has been reported to have a regulatory role in lung tumors and its interaction with FAK has been well-documented.[40] Additionally, PI3K signaling was shown to induce melanoma growth in mice upon dietary supplementation of chondroitin sulfate.[11b] To validate the role of PI3K in sulfation-mediated events, we generated PIK3CA-knockdown A549 cells (Figure S18, Supporting Information). PI3K loss caused a significant decrease in cell growth and cluster area in S-AlgLung hydrogels (**Figure 5**a,b). Furthermore, sulfation-induced upregulation of EMT-regulating transcription factors was lost (Figure 5c). Expression of E-cadherin was unchanged while N-cadherin was downregulated. On the other hand, fibronectin and vimentin did not show a decrease (Figure S19, Supporting Information). Stemness markers SOX2, OCT3/4, and CD133 were significantly downregulated upon PIK3CA knockdown in S-AlgLung hydrogels (Figure 5d). Thus, loss-of-function assessments revealed PI3K as an important regulator in the sulfation-induced growth, EMT and stemness of cells. To further confirm the involvement of PI3K, we performed gain-of-function experiments. We generated a PIK3CA-overexpressing A549 line (Figure S20, Supporting Information) and encapsulated in healthy-mimetic AlgLung hydrogels to investigate whether PI3K overexpression alone could mimic the effect of sulfation. In AlgLung hydrogels, PIK3CA overexpressing cells proliferated rapidly during the culture period, demonstrating the importance of this pathway in lung tumor cell growth (Figure 5e,f). Interestingly, even though proliferation was induced in AlgLung hydrogels, cellular morphology was quite different compared to sulfated hydrogels. PIK3CA-overexpressing cells displayed sheet-like growth, distinct from the cluster formation observed in S-AlgLung hydrogels (Figure 5e). Contrarily, the expression of EMT regulators that was upregulated upon sulfation was unchanged upon PIK3CA overexpression in AlgLung hydrogels (Figure 5g). In contrast, SLUG expression was significantly upregulated indicating that different transcription factors contribute to EMT in both contexts. Stemness markers were all significantly increased in AlgLung hydrogels demonstrating that PI3K activation alone was enough to induce stemness in lung tumor cells even in the absence of a sulfated microenvironment (Figure 5h). Next, we focused on the role of FAK in the PI3K-mediated effects of ECM sulfation. For this, we encapsulated PIK3CA-overexpressing cells in S-AlgLung hydrogels and treated them with an FAK inhibitor. Interestingly, PIK3CA-overexpressing cells demonstrated cluster formation in sulfated hydrogels as opposed to their behavior in AlgLung, however, FAK inhibition had no effect on cell growth (Figure 5i). Furthermore, expression of EMT markers were neither affected nor increased when FAK was blocked indicating that PIK3CA overexpression compensated for FAK inhibition, rendering the upstream role of FAK on sulfate-induced events (Figure 5j). Accordingly, our findings suggest that sulfation-promoted signaling follows the FGFR3-FAK-PI3K axis in lung tumor cells (Figure 5k).

2.6. Sulfated ECM Significantly Alters the Transcriptional Program of Cancer Cells

To elucidate a bigger picture of the molecular alterations that take place in response to increased sulfation in the ECM, we profiled transcriptomes of cells grown in AlgLung and S-AlgLung hydrogels with RNAseq. Principal component analysis showed unbiased separation of clusters (Figure S21, Supporting Information). We found 483 differentially expressed genes (DEGs) of which 277 genes were up-regulated and 206 were down-regulated in S-AlgLung compared to AlgLung (**Figure 6**a,b). Among the DEGs, strong upregulation of SNAIL and MUC5B was observed. DEGs were enriched in a variety of biological processes involved in multiple cancer types, cell cycle, ECM-receptor interactions, cytoskeleton organization and mucin-type glycan biosynthesis. This demonstrated a collective alteration in these pathways consistently with our results on the effect of sulfation on proliferation, invasion, stemness, RTK activation, and mucin expression (Figures S22–S25, Supporting Information). Understanding the causal connections between gene expression programs and cellular signaling pathways requires systems-based integrative approaches.[41] The precise mechanism through which alterations in ECM rewire signaling pathways remains poorly elucidated, particularly in the context of omics data analysis. Therefore, we combined transcriptional data analysis and network reconstruction to reveal the intermediate signaling mediators and signaling alterations induced by sulfated ECM. We successfully inferred the regulatory relationships between the DEGs and their corresponding transcription factors in sulfation-induced phenotype through statistical analysis and stringent filtering (see Experimental Section) and found 34 computationally identified transcription factors (Table S4 and Figure S26, Supporting Information). We then reconstructed a signaling network by orienting it from experimentally identified receptors, FGFR3 and RYK, as well as mediators, PIK3CA and PTK2 (FAK), to the inferred set of transcription factors that regulate the DEGs (Figure 6c). Reconstructed network revealed a more complete picture of the signaling events through adding the intermediate effectors besides the hits from the RNAseq data. Network analysis identified the interaction of RYK receptor with beta-catenin (CTNNB1) that plays a crucial role in lung cancer stem cell phenotype, in line with our experimental data demonstrating its elevated expression in S-AlgLung hydrogels (Figure 3f).[38] Moreover, MYC and MYCN, located downstream of PIK3CA in the reconstructed network, are known to be deregulated in lung cancer.[42] Activated MYC is an inducer of EMT which can interact with regulators including SNAIL and TWIST. Furthermore, MYC and PI3K-Akt signaling pathway have synergistical effect in enhancing tumor growth.[42] Gene set enrichment analyses on sulfated ECM-induced network revealed pathways regulating carcinogenesis of many cancer types, cell cycle, PI3K-Akt signaling and most interestingly PG signaling (Figure 6d). Intriguingly, when we compared the gene expression profile of PG+ patients in the TCGA LUAD cohort for the 483 DEGs between S-AlgLung and AlgLung

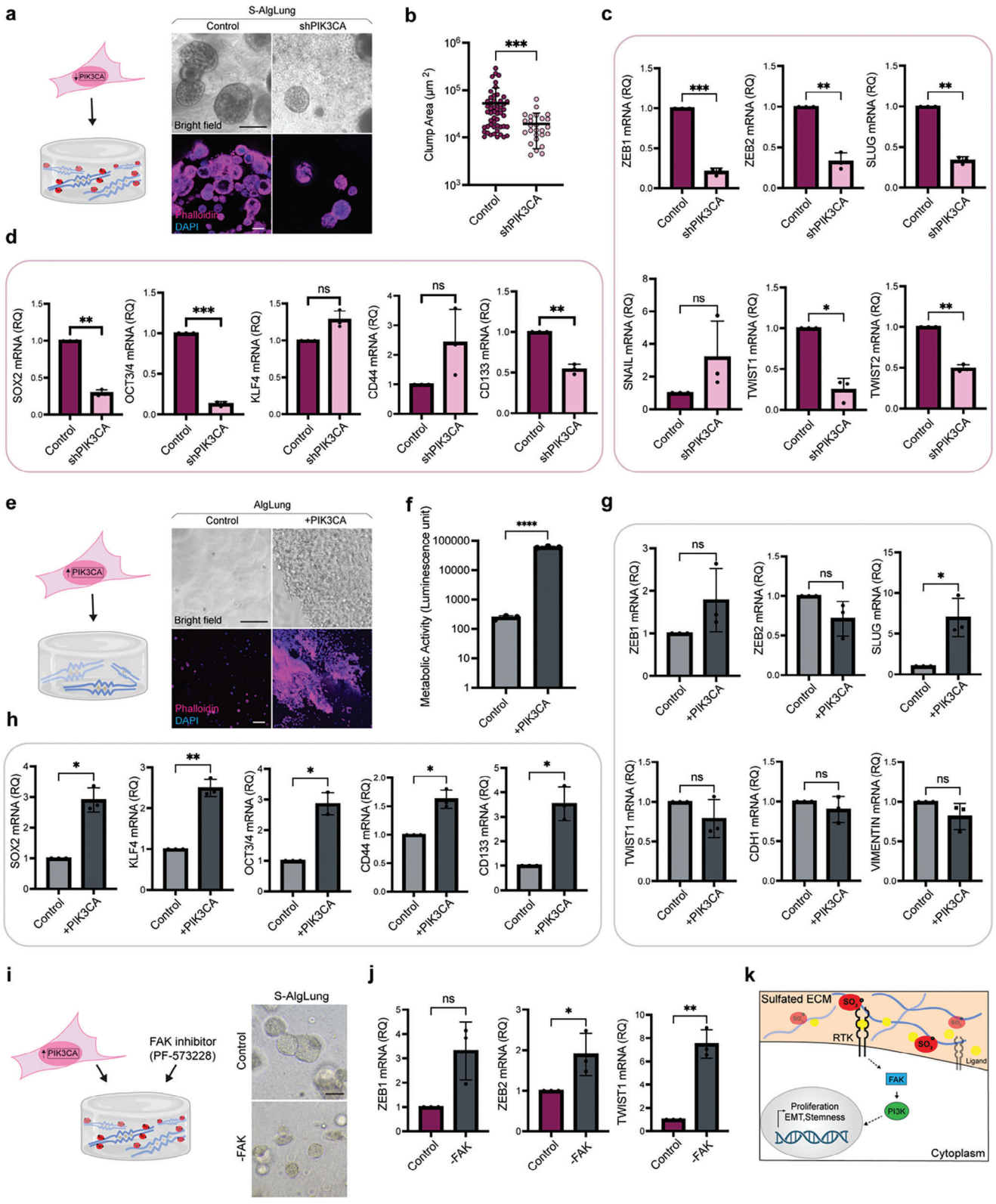

Figure 5. PI3K is a key regulator of sulfation-induced tumorigenic phenotype. a) Representative brightfield and confocal microscopy images of A549 cells expressing shPIK3CA or control vectors in S-AlgLung hydrogels. Cells were stained with phalloidin (magenta) and DAPI (blue), (scale bar: 100 μm). b) Quantification of cluster area (μm^2) of shPIK3CA-expressing A549 cells in S-AlgLung hydrogels compared to control, $^{***}p < 0.001$. c) mRNA expression of EMT regulators in shPIK3CA-expressing A549 cells grown in S-AlgLung hydrogels, ns not significant, $^{*}p < 0.05$, $^{**}p < 0.01$, $^{***}p < 0.001$. d) mRNA expression of stemness markers in shPIK3CA-expressing A549 cells grown in S-AlgLung hydrogels, ns not significant, $^{**}p < 0.01$, $^{***}p < 0.001$. e)

hydrogels, PG+ patient tumors clustered with S-AlgLung, further supporting the ability of our engineered sulfated hydrogels in representing PG-rich in vivo tumors (Figure 6e).

In line with this, PG+ patient tumors showed upregulation of CDK1 (Cyclin Dependent Kinase 1) in comparison to normal tissues (Figure 6f; Figure S30, Supporting Information). PTEN, a tumor suppressor and an antagonist of PI3K signaling, is another intermediate node in the network whose expression was significantly downregulated in PG+ tumors (Figure 6c,f; Figure S30, Supporting Information).[43] Interestingly, the only intermediate that did not show any change in PG+ patient tumors compared to healthy tissues was EGFR (Figure 6f; Figure S30, Supporting Information), supporting our experimental data which revealed robustness of sulfation-mediated growth and invasiveness against EGFR inhibition (Figure 3b–d).

3. Discussion

Lung cancer is a grave disease orchestrated by a complex series of molecular events in the TME. Emerging evidence suggest that alterations in ECM characteristics influence malignant transformation and progression.[2] There is a need for engineered models that can recapitulate the key aberrant changes in tumor matrices for elucidation of underlying signaling mechanisms.[2] Our findings reveal that expression of PGs is highly elevated among LUAD patients and correlates with invasive molecular programs including EMT and stemness. To mimic the increased PG and sGAG content in the TME, we developed a bioengineered human lung tumor model that allows tunability of sulfation within organotypic ECM. The use of decellularized native organ-derived ECMs offers the advantage of representing tissue-specific matrix onto which malignant characteristics can be introduced in a controlled manner. This is particularly important for modeling the aberrant changes in cell instructive ECM ligands considering the undefined composition of tumor-derived rBM materials. Native matrices allow the representation of the ECM at the tumor's site of origin as well as at site of metastasis using secondary organ-derived matrices. It has been established that controlling ECM ligand density is vital when modeling mechanical changes such as stiffness in engineered tumor tissues.[19] Similarly, control of mechanical properties is also very important when tuning aberrant biochemical content. Thus, our model allows recapitulation of sGAG increase in tumors while enabling independent control of ECM content, stiffness, viscoelasticity, and porosity. In this study, we used a stiffness range representing healthy lung tissue to focus on the sole effect of increased sulfation. However, our model allows future investigation of synergy between sulfation and stiffening, particularly since PGs can interact with mechanosensitive receptors to activate distinct signaling mechanisms.[21] Similarly, other aberrantly increased ECM ligands in tumors such as tenascin and fibronectin families as well as cell adhesive peptide sequences can be incorporated in the model for further complexifying.[6,44] Interestingly, sulfation alone induced remodeling in the ECM with elevated deposition of fibronectin and vimentin by lung tumor cells in our study. Moreover, expression of mucin-type glycans, crucial regulators of invasiveness and stemness in cancers, were stimulated upon sulfation.[33]

Our findings demonstrate that the sulfation state of the cellular microenvironment is a regulator of growth and invasive phenotype marked by activation of EMT and stemness in lung cancer cells. sGAG-mimetic alginate sulfate leads to activation of a specific set of RTKs (FGFR3 and RYK) in tumor cells and the downstream FAK-PI3K signaling axis. RTKs represent an important focus of targeted therapies, and compensatory activation of RTKs can contribute to therapeutic resistance.[45] Our findings suggest that blocking the activation of FGFR3 in lung tumors could be used as a therapeutic strategy. Moreover, modulating RYK function that has been shown to regulate stemness phenotype could enhance the efficacy of FGFR3 inhibition.[38] Combination therapies that target multiple RTKs as well as ECM remodeling enzymes such as heparanase can increase the efficacy of targeted therapies.[46] Therefore, tumor-mimetic models that allow investigation of complex RTK signaling can serve as a reliable preclinical platform for developing efficient treatment strategies. Transcriptomic analyses further confirmed that distinct molecular alterations occur in response to sulfation (Figure 6g). Our study employed network reconstruction of the transcriptomic landscape of tumor cells in engineered hydrogels. This way, transcriptomic data was integrated with experimentally identified source nodes that predicted intermediate effectors and regulatory signaling pathways that supported our hypothesis and findings. Among the signaling pathways enriched in S-AlgLung hydrogels are pathways involved in carcinogenesis, PI3K-Akt signaling and most interestingly PG signaling that exhibits that our engineered model successfully mimicked the PG-rich microenvironment of native tumors. Additionally, clustering of PG+ LUAD patient tumors with the transcriptomic profile of S-AlgLung poses an interesting aspect. Patient tumors represent a heterogeneous cast of cells, whereas our model entailed a single LUAD-derived cell line. This further emphasizes the importance of tumor ECM sulfation in determining the transcriptional programs that modulate growth and invasiveness. The fact that our enrichment analyses hit not only NSCLC but also many different types of

Representative brightfield and confocal microscopy images of A549 cells overexpressing PIK3CA or control vectors in AlgLung hydrogels. Cells were stained with phalloidin (magenta) and DAPI (blue), (scale bar: 100 µm). f) Metabolic activity analysis of PIK3CA-overexpressing A549 cells in AlgLung hydrogels using CellTiter-Glo 3D assay, $^{****}p < 0.0001$. g) mRNA expression of EMT regulators in PIK3CA-overexpressing A549 cells grown in AlgLung hydrogels, ns not significant, $^{*}p < 0.05$. h) mRNA expression of stemness markers in PIK3CA overexpressing A549 cells grown in AlgLung hydrogels, $^{*}p < 0.05$, $^{**}p < 0.01$. i) Representative brightfield images of PIK3CA-overexpressing A549 cells grown in S-AlgLung hydrogels and treated with FAK inhibitor (scale bar: 100 µm). j) mRNA expression of EMT regulators in PIK3CA-overexpressing A549 cells grown in S-AlgLung hydrogels and treated with FAK inhibitor, ns not significant, $^{*}p < 0.05$, $^{**}p < 0.01$. k) Schematic illustration of the sulfated ECM-induced signaling cascade in lung tumor cells grown in S-AlgLung hydrogels. Sulfated ECM exerts affinity to bioactive ligands that leads to the activation of FGFR3 and RYK receptors and their downstream signaling. PI3K acts as a hub in sulfation-induced proliferation, EMT activation and stemness phenotype in A549 cells. All quantitative data is represented as mean ± S.D and statistical significance was analyzed using an unpaired, two-tailed student's *t*-test. In qRT-PCR data, relative quantification (RQ) was used with normalization to control group.

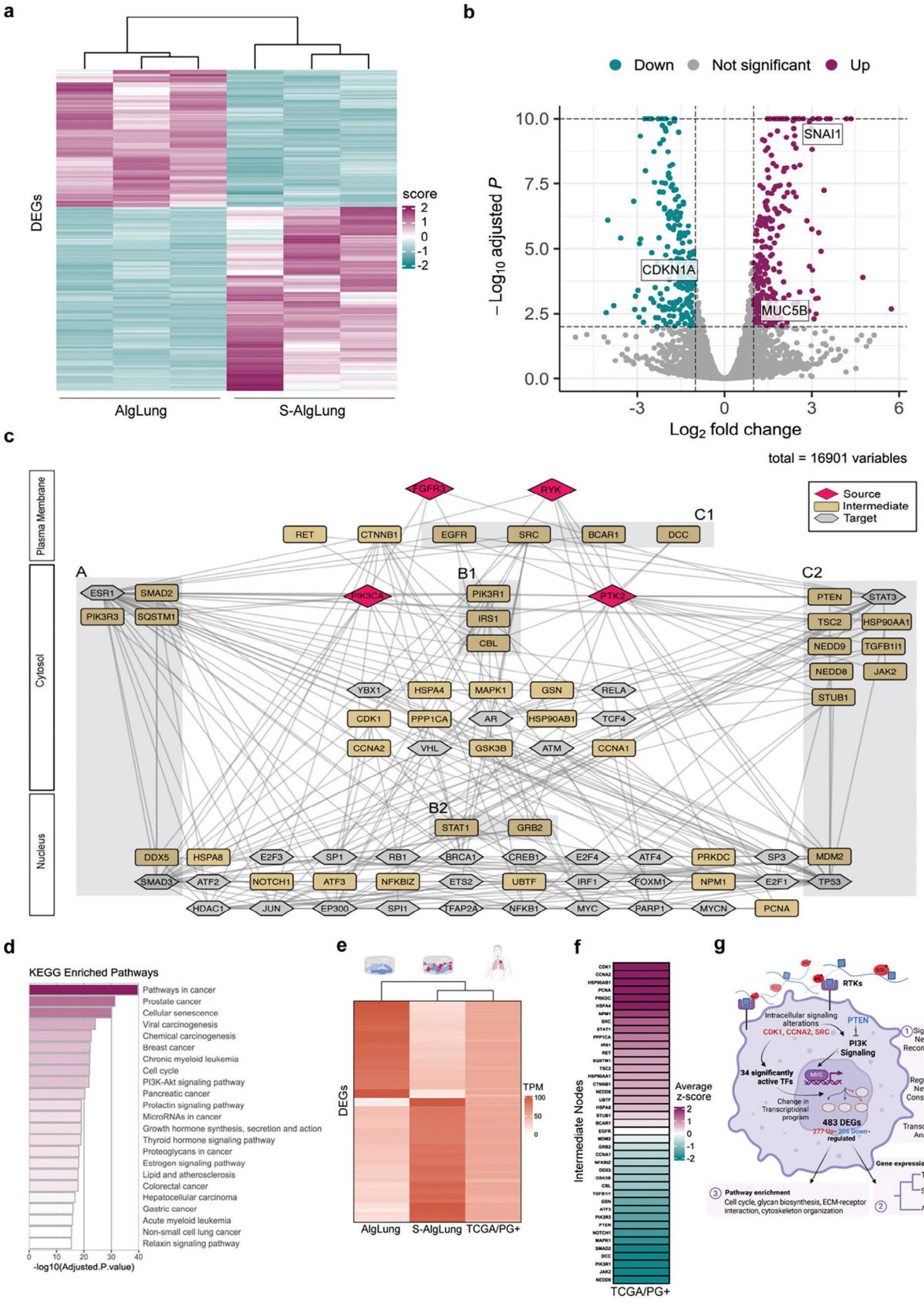

cancers (prostate, gastric, breast, myeloid leukemia) underlines that sulfation is a critical pan-cancer ECM characteristic and suggests that our model can be expanded to different tumors. Last, these approaches that entail tunability and customization of engineered tumor models can be adapted to patient-derived organoids for testing therapeutics as a further step toward precision medicine.

4. Experimental Section

Bioinformatics Analyses for Publicly Available Patient Data: The cBioPortal database was used to download the human lung cancer data of LUAD (TCGA, PanCancer Atlas), and LUAD (CPTAC, Cell 2020 datasets).[47] From the LUAD TCGA datasets, mRNA expression z-scores relative to normal samples (log RNA Seq V2 RSEM) dataset were utilized (Figure 1a). A list of PG genes was obtained from the Matrisome Database, with 34 genes being present in the TCGA dataset (Table S2, Supporting Information). The pairwise correlation among these genes were visualized in a heatmap using ComplexHeatmap (v2.13.1) in R (https://cran.r-project.org /package = BiocManager, https://www.R-project.org).[48] Highly expressed PG gene names were identified, and correlation values were hierarchically clustered both by rows and columns. TCGA LUAD samples were divided into two groups as (PG+) and negative (PG-), respectively, based on the overexpression of PG genes in tumors compared to normal samples. Tumors with at least three PG genes being significantly deviating from the mean expression of normal samples (z-score ≥ 3.0) were defined as PG+ while tumors not exhibiting a significant change in any PG genes were defined as PG-. The cutoff of 3.0 for z-scores is a commonly used statistical threshold to identify significant deviations from the mean. The rationale for using at least three genes for PG+ definition is to ensure that the comparison between groups is robust and meaningful. Including patients with overexpression in only one or two genes may lead to random variability, creating a "gray zone." By setting a threshold of at least three overexpressed genes, the risk of random comparisons is minimized and patients with a more definitive pattern of gene overexpression are focused on, thereby enhancing the reliability of the analysis. Scores were derived via computation of the average expression of genes in the relevant list for each patient sample. A comparison between the PG scores of PG+ and PG- samples was conducted to assess significant differences between the two groups (Figure 1c). The result was shown as a box plot generated with the help of ggpubr of R (v0.6.0) (https://cran.r-project.org/ package = ggpubr, https://www.R-project.org). Besides the PG genes, literature-curated list of EMT, invasiveness-associated and CSC genes, respectively (Table S2, Supporting Information), was gathered.[49] A score function was defined to summarize the collective activity of a specific gene set per patient. Thus, the activity of EMT, PG, and CSC gene sets can be inferred from their collective behavior. By averaging the z-scores of the genes in a set, this score indicated whether the mean deviation of the gene group was in the direction of upregulation or downregulation in tumors compared to normal tissues. The score function is as follows;

$$score\ (i,j) = \frac{\sum_{k=1}^{n} z_k}{n} \quad (1)$$

where i is the gene set (PG, EMT, CSC, or any other sets), n is the number of genes in the set, z_k is the z-score of the gene k in the patient sample j.

Each score category (PG-, EMT, Invasiveness-, CSC-scores) represents the combined activity of the corresponding gene group. These scores were used to be indicators of sulfation potential (PG-score), invasiveness (EMT- and Invasiveness-score), and stemness (CSC-score) properties of each tumor rather than any single gene. Two regression plots were generated to visualize the relationship between EMT scores and PG scores with the same samples on both TCGA LUAD transcriptomic and CPTAC LUAD proteomic data using the PG and EMT gene list in Table S2 (Supporting Information) (Figure 1e,f). For the CPTAC LUAD data, the average of the z-scores of protein abundance ratios was used to calculate the EMT and PG scores with the same gene lists mentioned. Regression plots were created using Python's seaborn (v0.12.0) (https://pypi.org/project/seaborn/). Spearman rank correlation was employed to calculate correlation values. TCGA LUAD clinical patient and clinical sample datasets were used to conduct a survival analysis (Figure 1d). The ggfortify package in R (v0.4.14) was used to generate the survival plot (https://cran.r-project.org/web/packages = ggfortify, https://www.R-project.org).

sGAG Quantification: 5 NSCLC LUAD samples and their normal parenchyma counterparts (Table S3, Supporting Information) were collected with Koc University Institutional Review Board (2020.001.IRB2.001) ethics approval and consent of participants undergoing lobectomy as part of their clinical care. Quantification of sGAG content was performed using Blyscan Sulfated Glycosaminoglycan Assay kit (Biocolor, UK) following manufacturer's instructions. Briefly, weighed tumor and normal parenchyma samples were digested in papain (Sigma) buffer (125 µg mL^{-1}) including sodium acetate (400 mg), EDTA (200 mg) and cysteine (50 mg) in 0.2 M sodium phosphate buffer (50 mL) at pH 6.4. at 65 °C overnight. Samples were then mixed with dye reagent followed by dye retrieval and absorbance measurement at 656 nm using a microplate reader. sGAG content in tumor and normal parenchyma samples were normalized to their wet weight.

Tissue Histology: NSCLC LUAD tumor and matched normal parenchyma tissue samples were fixed with formaldehyde solution (3.7%, EMS) at 4 °C overnight, followed by immersion in sucrose (30%) overnight. Samples were then embedded in OCT (Tissue-Tek), snap-frozen, sectioned as 10 µm slices and mounted on glass slides. For haematoxylin & eosin staining, slides were hydrated and stained with Mayer's Haematoxylin (Merck) for 3 min followed by a 3-min wash with tap water. Then, slides were immersed in ethanol (95%) and stained with Eosin solution (Bright-Slide) for 45 s. To visualize deposition of sGAGs in samples, slides were hydrated and stained with Alcian Blue (1%, Sigma) in acetic acid solution (3%) at a final pH of 2.5 for 30 min followed by a

Figure 6. Sulfated ECM significantly alters the transcriptional program of cancer cells. a) Heatmap shows hierarchically clustered normalized expression values of differentially expressed genes across samples. Negative z-scores are in blue color-scale, and positive z-scores are in purple color-scale. b) Volcano plot shows DEGs in purple (up-regulated genes), blue (down-regulated genes), and gray (other genes). Thresholds to find DEGs (adj-pvalue<0.01 and abs(log2(FC))>1) are shown as black dashed horizontal and vertical lines. c) Reconstructed signaling network orients from receptors to significant transcription factors that regulate the differentially expressed genes. In this network, RYK, FGFR3, PTK2, and PIK3CA are source nodes and significant transcription factors are target nodes. Pathlinker is used for network reconstruction. d) Bar plot shows the functionally enriched KEGG pathways of intermediate nodes. P-values were determined using a hypergeometric test. e) Heatmap shows TPM-normalized values of 483 DEGs, comparing TCGA/PG+ samples with S-AlgLung and AlgLung samples. Hierarchical clustering reveals that patient samples are more closely related to S-AlgLung samples. f) Average z-scores of mRNA expression data of intermediate nodes in TCGA/PG+ samples. Negative z-scores are in blue color-scale, and positive z-scores are in purple color-scale. g) Schematic summary of the results from our three-step computational pipeline (RNA-seq data analysis, identifying significant transcription factors and reconstructing signaling network) used for integrative network modeling (label 1). ECM-cell interactions, influenced by sulfation, initiate a cascade of signaling events. The reconstructed signaling network promotes 34 significantly active transcription factors, including MYC, leading to widespread changes in the transcriptional program of the cells. These changes result in the differential expression of 483 genes (DEGs), with 277 genes being upregulated and 206 downregulated. Importantly, the DEGs are more highly correlated with patient tumor data in sulfated ECM compared to non-sulfated ECM (label 2). Pathway enrichment analysis on sulfated ECM-induced network revealed pathways regulating cell cycle, glycan biosynthesis, ECM-receptor interaction, and cytoskeleton organization (label 3).

2-min wash with tap water. After staining, all slides were dehydrated with graded alcohol treatments, mounted, and visualized by light microscopy.

Modification of Alginate: Sulfation of alginate (Novamatrix) was carried out as previously described.[15a] Briefly, chlorosulfonic acid (99%, Sigma) was diluted in formamide (Sigma) at a final concentration of 2% and added dropwise onto alginate while stirring. The reaction was carried out at 60 °C with agitation for 2.5 h. Alginate sulfate was precipitated with cold acetone and re-dissolved in ultra-pure water and neutralized overnight. The solution was purified by dialyzing in 12 kDa molecular weight cut-off (MWCO) dialysis tubing (Sigma) against sodium chloride (100 mmol) for 48 h and ultra-pure water for 72 h with solution change every 12 h and then lyophilized.

Chemical Characterization of Alginate Sulfate: Elemental analysis of sulfur content in alginate sulfate was performed using high-resolution inductively coupled mass spectrometry (ICP-MS). Degree of sulfation (DS), the number of sulfate groups per monomer, was estimated from the mass balance equation assuming one sodium counterion for each negatively charged group and one water molecule per monosaccharide:

Monosaccharide mass = $C_6O_6H_5$ + (DS+1) Na^+ + (DS) SO_3^- + H_2O.

Molecular weight of alginate sulfate was analyzed by size exclusion chromatography with a multiangle laser light detection system (SEC-MALS) using a refractive index (dn/dc) of 0.15 for all samples.

Decellularization and Characterization of Lung Tissues: Decellularization of bovine lung was carried out as previously described.[14] Briefly, lung tissue pieces were thoroughly washed in dH_2O with Penicillin/Streptomycin/Amphotericin (2%) and then subjected to freeze-thaw cycles using liquid nitrogen. Next, tissue pieces were treated with DNase (10U ml^{-1}, Sigma), washed again in dH_2O, lyophilized and, cryomilled into a powder form. dECM powder was then digested in pepsin solution (1 mg ml^{-1}, Sigma) at a final concentration of 15 mg ml^{-1} (w/v) at room temperature for 48 h, neutralized, lyophilized, and stored at −20 °C for further use. To validate elimination of cellular content in decellularized bovine lung (dLung), samples were fixed in formaldehyde solution (3.7%), embedded in OCT, cryo-sectioned and mounted on glass slides. Haematoxylin & Eosin and Hoechst staining was performed as previously described.[14] To characterize collagen and sGAG content, Sirius red and Alcian blue stainings were performed, respectively, as previously described.[14]

Cell Culture: Human LUAD cell line A549 (#CCL-185) was purchased from American Tissue Culture Collection (ATCC) and cultured in growth medium DMEM/F12 (Lonza) supplemented with FBS (10%, Biowest) and PenStrep (1%, Gibco). Human embryonic kidney (HEK293T) cells were cultured with DMEM High Glucose (Biowest) supplemented with FBS (10%) and PenStrep (1%). Both cell lines were maintained in an incubator at 37 °C and 5% CO_2 and tested for Mycoplasma using MycoAlert Mycoplasma Detection Kit (Lonza) regularly.

Hydrogel Formation and Cell Encapsulation: Alginate and alginate sulfate were dissolved in serum-free DMEM/F12 and sterile filtered using 0.2 µm pore size syringe filter. Lyophilized dLung was also dissolved in serum-free DMEM/F12 containing PenStrep (2%) overnight at 4 °C. All hydrogels consisted of Alg/S-Alg (10 mg ml^{-1}) and dLung(5,4 mg ml^{-1}) throughout the study. Calcium sulfate stock solution was prepared in ddH_2O and autoclaved. Calcium sulfate solutions in serum-free DMEM/F12 were prepared at working concentrations (120-480 mmol). Before the cell encapsulation in hydrogels, A549 cells were expanded as monolayer cultures, trypsinized, centrifuged, counted, and resuspended in growth medium. The final cell density in hydrogels was $5*10^4$ ml^{-1} unless stated otherwise. While keeping all materials on ice, the required amount of calcium sulfate solution was transferred to a 1 mL Luer lock syringe. Next, Alg/S-Alg, dLung and cell suspension were pipetted into another syringe and mixed uniformly without forming bubbles. Then, two syringes were connected using a female-female Luer lock coupler, and solutions were mixed rapidly before hydrogels were deposited into a 24-well plate. Hydrogels were allowed to solidify for 45 min in an incubator before adding culture medium. Alginate-Matrigel (Growth Factor Reduced, Corning) (AlgMat) hydrogels were prepared following a similar approach.

Mechanical Characterization: Mechanical characterization of hydrogels was performed using a Discovery HR-2 rheometer (TA instruments). Briefly, hydrogels were deposited onto the lower plate which was precooled to 4 °C and a 20 mm parallel plate was lowered until the gap reached 1 mm. Mineral oil (Sigma) was applied at the periphery of the gels to prevent dehydration during the measurement. Oscillatory rheology was used to measure the storage modulus at constant frequency and amplitude (1 Hz, 1% strain) for 2 h. For viscoelasticity measurements, creep-recovery test was performed with application of a constant shear stress of 20 Pa for 1 h on gels while strain was recorded. Then, the sample was unloaded, and the strain was measured for 2 h. All measurements were done at least in triplicates.

Hydrogel Porosity Assessment: Rhodamine-tagged dextran (Invitrogen) was encapsulated into AlgLung and S-AlgLung hydrogels at a concentration of 0.5 mg ml^{-1}. Two different molecular weights (10 kDa/70 kDa) were used for dextran. Hydrogels were cast on a 24-well plate and incubated in PBS for 3 days. Media was removed every 24 h for measuring the diffusion of rhodamine. Quantification of released dextran was performed with fluorescence readout using a microplate reader at 570 nm/590 nm excitation/emission. At least three replicates were used for each condition.

Quantification of DNA: dsDNA quantification from hydrogels was performed by Quant-iT PicoGreen dsDNA Assay Kit (Invitrogen) according to manufacturer's instructions. Briefly, at designated time points, hydrogels were collected, washed once with a wash buffer containing sodium chloride (150 mmol) and calcium chloride (5 mmol) and stored at −80 °C until the assay was carried out. Hydrogels were digested in papain buffer (125 µg mL^{-1}) consisting of EDTA (10 mmol), sodium phosphate (100 mmol), sodium acetate (100 mmol), L-cysteine (10 mmol) at a pH of 6.4 at 60 °C overnight. After digestion, diluted samples were mixed with Quant-iT PicoGreen reagent and incubated for 5 min at room temperature. Fluorescence was measured at 520 nm with excitation at 485 nm in a microplate reader. Experiments were done using at least three hydrogels for each group.

CellTiter-Glo 3D Cell Viability Assay: CellTiter-Glo 3D Cell Viability Assay (CTG) (Promega) was performed in hydrogels according to manufacturer's instructions with minor modifications. Hydrogels were briefly washed and incubated with assay buffer for 45 min at room temperature after a 5-min shake in a plate shaker. Luminescence was measured for at least 3 hydrogels using a microplate reader.

Assessment of Cell Viability and Morphology: A549 cells encapsulated in hydrogels were stained at the beginning (Day 7) and the end of culture (Day 28) with Calcein-AM (2 µM, Invitrogen) and propidium iodide (30 µg mL^{-1}, Sigma) in growth medium to assess viability. To monitor the morphological changes of encapsulated A549 cells in hydrogels, samples were fixed with paraformaldehyde (4%) for 30 min at room temperature. The gels were then washed with a wash buffer three times for 5 min followed by permeabilization and blocking in BSA (5%, Sigma), Triton X-100 (1%, Sigma) for 1 h at room temperature. F-actin staining was performed using Phalloidin-iFluor 488 Reagent (1:1000, Abcam) for 45 min at room temperature followed by a 5-min wash. Nuclei staining was performed with DAPI (1 µg mL^{-1}, Sigma) and samples were washed twice with wash buffer for 10 min before imaging. Samples were imaged with Leica SP8 confocal microscope and z-stacks were obtained with a 5 µm step length for at least three hydrogels.

Clump Analysis: Clump area and invasiveness of clumps formed in hydrogels that were stained for F-actin and nuclei were analyzed using ImageJ. For each condition, at least three hydrogels were imaged and at least 5 z-stack images were analyzed. Briefly, z-stack images were projected with maximum intensity, thresholded, then boundaries of clusters were calculated using the "analyze particles" module. In some images, clumps were overlapped making it hard to analyze the individual clumps. In these cases, z-stack slices were individually analyzed, and total clump numbers were normalized to the total stack number. Invasiveness of clumps was calculated using the circularity output from the cluster size analysis. A circularity value of one obtained from analysis indicates a perfect circular cell clump which shows 0% invasiveness whereas a value of zero circularity indicates 100% invasiveness.

Immunofluorescence: Hydrogels were fixed with paraformaldehyde (4%) for 30 min at room temperature. Next, the gels were washed with a wash buffer three times for 5 min followed by permeabilization and block-

ing in goat serum (5%, Gibco), BSA (1%), Triton X-100 (1%) for 1 h at room temperature. Primary antibody incubation was performed overnight at 4 °C in a staining buffer containing BSA (1%), Triton X-100 (0.1%). Primary antibodies used for these studies are listed in Table S5 (Supporting Information). Hydrogels stained with primary antibodies were washed twice for 10 min at room temperature with staining buffer. Secondary antibody incubation was performed overnight at 4 °C using goat anti-rabbit FITC (1:200, H&L, Jackson ImmunoResearch) or goat anti-mouse Alexa Fluor 633 (1:200, H&L, Invitrogen) followed by 2 h wash with staining buffer at room temperature. Nuclei staining was performed with DAPI (1 µg mL^{-1}) in a staining solution followed by a 15-min wash with staining buffer. Samples were imaged with Leica SP8 confocal microscope.

Phospho-RTK Array: Phosphorylation of RTKs in A549 cells encapsulated in hydrogels was revealed by Proteome Profiler Human Phospho-RTK Array (R&D) according to manufacturer's instructions. Briefly, AlgLung and S-AlgLung hydrogels were treated with a cell retrieval buffer containing sodium citrate (100 mmol), EDTA (50 mmol) in ddH_2O, at a final pH of 7.2 to retrieve cells from the hydrogels. After two washing steps for 5 min with ice-cold PBS, cell lysates were collected by a lysis buffer provided in the kit and quantified with BCA Protein Assay. Arrays were incubated with 100 µg of total protein for both conditions. Images were captured by LI-COR imaging system Odyssey Fc with Image Studio Acquisition Software. The quantification of each dot was performed using the longest exposed images by ImageJ and the expression of p-RTKs in S-AlgLung hydrogels was normalized to AlgLung samples.

Inhibition Assays: Drug inhibitors and antibodies with the indicated concentrations found in Table S6 (Supporting Information) were added in the culture medium of hydrogels at day 4 and renewed every 3 days until day 21.[15a,50] Same amount of DMSO was also added in the culture medium as a control group. At the end of the experiment, three hydrogels were kept for DNA quantification or CTG analysis in each group, and the remaining hydrogels were fixed and stained for F-Actin as previously described in the text to analyze cluster morphologies.

Hanging Drop Assay: A549 cells cultured as monolayers were trypsinized, and the final concentration of cells was adjusted to 2×10^5 cells mL^{-1}. Cells were placed as 10 uL drops onto an inverted lid, and the bottom chamber of the 60 mm petri dish was filled with 10 mL of PBS. Then, the lid was carefully inverted onto the PBS-containing bottom chamber, and drops were incubated at 37 °C, and 5% CO2 for 3 days. Following, spheroids were collected and encapsulated into AlgLung and S-AlgLung hydrogels according to the hydrogel generation protocol given in detail above. Gels were cultured and monitored for 3 weeks, and the bright field images of spheroids were captured.

Transwell Migration Assay: A549 cells in the density of 10^5 mL^{-1} were encapsulated in AlgLung and S-AlgLung hydrogels and cultured in the upper chamber of an 8-µm pore size inserts (Corning) in a 24-well plate with culture medium. At day 21, glass coverslips at the bottom of the 24-well plate were fixed using 4% PFA in PBS for 15 min, then nuclei staining was performed with DAPI and samples were visualized.

Plasmid Constructs: Full length plasmid of PI3KCA (phosphatidylinositol-4,5-biphosphate 3- kinase catalytic subunit alpha, NM_0 06218.4) was purchased from Addgene (Plasmid ID: 81 736, Hahn and Root Lab). The coding sequence of PI3KCA was cloned into Lenti-PCDH-EF1-mNeonGreen-MCS-T2A-puromycin plasmid (a kind gift from Fırat-Karalar Lab, Koç University, Istanbul). GFP-tagged shRNA plasmids targeting PI3KCA(NM_0062) and scrambled shRNA plasmid were obtained from Vector Builder (plasmid IDs: VB9000558918GSY, VB9000619992CNJ and VB9000558929 respectively).

Restriction Enzyme Cloning and Primers: PI3KCA open reading frame was cloned into PCDH-mNeonGreen backbone with restriction-dependent cloning. Phusion High Fidelity DNA Polymerase (NEB) was used with the following primers: PI3KCA_human_forward_BamH1 5′-ACTGGGATCCATGCCTCCACGACCATCATC-3′; PI3KCA_human_reverse_Not1: 5′-ACTGGCGGCCGCGTTCAATGCATGCTGTTTAATTGTG-3′. The PCR reaction was performed and the resulting PCR product as well as PCDH-mNeonGreen-MCS-T2A-puromycin plasmid were cleaved with BamH1(NEB) and Not1(NEB) enzymes. Digested products were then ligated with T4 DNA Ligase (NEB).

Lentiviral Production and Stable Line Generation: HEK293T cells were transfected with Lipofectamine 3000 Transfection Reagent (Invitrogen) with a ratio of 4:3:1 for Lentiviral DNA, psPAX2, PCMV-VSVG respectively. 48 h post-transfection viral supernatants were collected and concentrated with PEG8000 (Sigma). A549 cells were transduced with lentiviral particles expressing the gene of interest with an exogenous fluorescent tag with a MOI of 5. For enhancing the infection efficiency, Protamine Sulfate (10 µg mL^{-1}, Sigma) was used. Cells were selected with Puromycin (1.5 µg mL, Sigma) for 5 days.

Sorting of PI3KCA-Overexpressing Cells: A549 cells transduced with mNeonGreen-PI3KCA viral plasmids were sorted utilizing Attune NxT Flow Cytometer to establish a homogenous PI3KCA-overexpressing population. Cells were trypsinized and centrifuged at 300 g for 5 min. Supernatant was removed carefully, and pellet was resuspended with Magnesium and Calcium free PBS supplemented with BSA (3%). Cell suspension was run through a strainer with 40 µm mesh size to obtain a single cell suspension. FSCA versus SSC and FSCH versus FSCA gates were applied to separate single cells and eliminate doublets. Then, mNeonGreen-expressing transduced cells were sorted with FITCA versus FSCH.

Western Blotting: Protein isolation from hydrogels is carried out in two steps. Briefly, cells are first harvested from hydrogels by crushing gels with cell retrieval buffer containing sodium citrate (100 mmol), EDTA (50 mmol) in ddH_2O, at a final pH of 7.2. Following, the cell pellet was lysed with RIPA buffer (EcoTech) supplemented with PhosSTOP (Roche) and cOmplete Mini-EDTA Free (Roche) for 40 min on ice. The protein concentration was determined with BCA Protein Assay (Pierce). 50 µg protein was loaded in each well of precast 4–15% Bis Tris gels (BioRad) and run for 2 h at 80 V. Wet transfer was performed onto a PVDF (BioRad) membrane for 2 h at 110 V. Membrane was washed with Tris-Buffered Saline with Tween-20 (TBST) for three times. Blocking was performed with 5% non-fat dry milk (BioRad) and incubated at 4 °C overnight. The membrane was washed with TBST for three times. Primary antibodies were prepared as follows: FGFR3(#A0404, Abclonal) at 1:1000, pFGFR3(#Ap1274, Abclonal) at 1:1000, PI3KCA (p110a) (#A0265, Abclonal) at 1:500, GAPDH (#AB9485, Abcam) at 1:1000 in TBST with BSA (5%, Sigma) and Sodium Azide (0.02%, Sigma) and incubated at 4 °C overnight. Membrane was washed with TBST three times. Secondary antibody was prepared as follows: Rabbit IgG H&L (HRP) (#ab97051, Abcam) at 1:10 000 dilution in TBST with 5% non-fat milk and incubated for 45 min at room temperature. After incubation, membranes were washed with TBST and incubated with a highly sensitive ECL solution (Pierce) for chemiluminescence detection. Visualization was performed with LI-COR imaging system Odyssey Fc with Image Studio Acquisition Software.

Real Time-Quantitative Polymerase Chain Reaction (qRT-PCR): RNA extraction from hydrogels was performed with TRIzol Reagent (Invitrogen). After adding TRIzol, the gels were crushed with a pestle on dry ice, then centrifuged at 12000 rpm for 5 min at 4 °C. Chloroform was added to the supernatant and incubated on ice for 10 min followed by centrifugation at 12000 rpm for 15 min at 4 °C. Aqueous phase was collected and equal volume ethanol (70%) was added. From this point, RNA isolation was performed with Nucleospin RNA II (MN) kit following manufacturer's instructions. 1 µg RNA was reverse-transcribed using M-MLV Reverse Transcriptase Kit (Invitrogen). qRT-PCR was performed using SYBR Green (Roche) on a LightCycler (Roche) equipment. Primer sequences that were used are given in Table S7 (Supporting Information).

Transcriptomic Analyses and Network-Based Data Integration: RNAseq was performed using DNBSEQ Platform by BGI Genomics (Hong Kong). The quality of the reads was checked using FastQC and mapped against the ENSEMBL Homo Sapiens reference genome (GRCh38) using STAR version 2.7.3a.[51] Counts were calculated from the aligned reads using the featureCounts function of the Rsubread R package.[52] Differential analysis and normalization were performed using the DESeq2 R package and R (version 4.2.2).[53] Genes with more than ten reads were used in the DESeq2 analysis. Additional filtering of genes with extreme count outliers and low mean normalized counts was performed by DESeq2, yielding 16 901 genes. For the representation of gene abundance transcripts per million (TPM) values were computed using DGEobj.utils R package. Genes were considered differentially expressed when log2 fold changes

were equal or greater than 1.0 for upregulated genes or equal or lower than −1.0 for downregulated genes, with a Benjamini–Hochberg p-adjusted value less than or equal to 0.01. For functional enrichment analysis of GO Biological Process and KEGG Datasets, EnrichR was used.[54] For gene-set enrichment analysis for GO Biological Process, WebGestalt[64] was used. A signaling network was reconstructed using PathLinker version 1.4.3 in Cytoscape version 3.8.2 where iRefWeb was selected as the reference interactome.[55,56] Protein-protein interactions that have a confidence score of less than 0.4 were filtered out from the iRefWeb interactome. Additionally, UBC and its interactions were deleted. Filtered iRefWeb interactome was used as the reference interactome, "undirected" and "unweighed" parameters were selected, and iterations were made with the given source and target nodes with a k value of 1000. Obtained subnetwork (226 nodes, 754 edges) was used as a reference, "undirected", "weights are probabilities = confidence", and "edge penalty = 1" parameters were selected and iterations were made without changing source and target nodes with a k value of 50000. After this iteration, a subnetwork (77 nodes, 258 edges) was obtained. The network was visualized with information on the source, target, and subcellular locations.

Supporting Information

Supporting Information is available from the Wiley Online Library or from the author.

Acknowledgements

The authors acknowledge funding from the International Fellowship for Outstanding Researchers Program of TÜBİTAK (118C238), European Union's Horizon 2020 research and innovation program under the Marie Skłodowska-Curie grant agreement 101032602, and Swiss National Science Foundation (P2EZP2-172172). The entire responsibility of the publication belongs to the owner, the financial support from TÜBİTAK does not mean that the content of the publication is approved in a scientific sense by TÜBİTAK. BioRender.com was used to create the illustrations in Figures 2a,3c,5 and ToC figure. The authors gratefully acknowledge the use of services and facilities of Koç University Research Center for Translational Medicine (KUTTAM).

Conflict of Interest

The authors declare no conflict of interest.

Author Contributions

A.K. and D.O. contributed equally to this work. E.Ö. conceived the project and designed the research. N.T., G.V.N., I.S., and S.D. provided insights on research design. N.T., A.D., and C.U. performed bioinformatics analyses and network modeling. P.F., P.B., S.T., S.E., and S.D. provided clinical samples and performed histopathological assessments. Ø.A. helped with ICP-MS and SEC-MALS analyses. K.C., I.C.K., and S.K. provided technical support in experiments. A.K., D.Ö., S.N.Ö., S.S., K.Y., S.Ö., D.T.S., N.S., and E.D., conducted experiments. A.K., D.Ö., and E.Ö analyzed data and wrote the manuscript.

Data Availability Statement

The results shown here are in part based upon data generated by the TCGA Research Network: https://www.cancer.gov/tcga. The CPTAC LUAD dataset is available from the CPTAC Portal (https://pdc.cancer.gov/pdc/study/PDC000153). The cBioPortal database was used to download the gene expression (TCGA), and proteomic (CPTAC) datasets of the human LUAD tumors. For RNA sequencing data generated in the study: both raw and processed RNA-seq data for each sample is publicly available in Gene Expression Omnibus (https://www.ncbi.nlm.nih.gov/geo/). The codes to reproduce the analysis and generate the figures of computational analyses are available upon request from the corresponding author.

Keywords

cancer, extracellular matrix (ECM), hydrogels, tissue engineering, tumor microenvironment (TME), tumor models

Received: December 19, 2023
Revised: July 8, 2024
Published online: July 31, 2024

[1] D. Hanahan, R. A. Weinberg, *Cell* **2011**, *144*, 646.
[2] T. Cox, *Nat. Rev. Cancer* **2021**, *21*, 217.
[3] M. T. Kozlowski, C. J. Crook, H. T. Ku, *Commun. Biol.* **2021**, *4*, 1387.
[4] R. Parenteau-Bareil, R. Gauvin, F. Berthod, *Materials* **2010**, *3*, 1863.
[5] a) U. Freudenberg, Y. Liang, K. L. Kiick, C. Werner, *Adv. Mater.* **2016**, *28*, 8861; b) A. V. Taubenberger, L. J. Bray, B. Haller, A. Shaposhnykov, M. Binner, U. Freudenberg, J. Guck, C. Werner, *Acta Biomater.* **2016**, *36*, 73; c) V. Kast, A. Nadernezhad, D. Pette, A. Gabrielyan, M. Fusenig, K. C. Honselmann, D. E. Stange, C. Werner, D. Loessner, *Adv. Healthcare Mater.* **2023**, *12*, 2201907; d) C. R. Below, J. Kelly, A. Brown, J. D. Humphries, C. Hutton, J. Xu, B. Y. Lee, C. Cintas, X. Zhang, V. Hernandez-Gordillo, L. Stockdale, M. A. Goldsworthy, J. Geraghty, L. Foster, D. A. O'Reilly, B. Schedding, J. Askari, J. Burns, N. Hodson, D. L. Smith, C. Lally, G. Ashton, D. Knight, A. Mironov, A. Banyard, J. A. Eble, J. P. Morton, M. J. Humphries, L. G. Griffith, C. Jorgensen, *Nat. Mater.* **2022**, *21*, 110.
[6] G. Burgstaller, B. Oehrle, M. Gerckens, E. S. White, H. B. Schiller, O. Eickelberg, *Eur. Respir. J.* **2017**, *50*, 1601805.
[7] S. H. Kim, J. Turnbull, S. Guimond, *J. Endocrinol.* **2011**, *209*, 139.
[8] Z. Du, C. M. Lovly, *Mol. Cancer* **2018**, *17*, 58.
[9] D. Soares da Costa, R. L. Reis, I. Pashkuleva, *Annu. Rev. Biomed. Eng.* **2017**, *19*, 1.
[10] a) N. Afratis, C. Gialeli, D. Nikitovic, T. Tsegenidis, E. Karousou, A. D. Theocharis, M. S. Pavao, G. N. Tzanakakis, N. K. Karamanos, *FEBS J.* **2012**, *279*, 1177; b) A. D. Theocharis, N. K. Karamanos, *Matrix Biol.* **2019**, *75-76*, 220; c) C. Marques, C. A. Reis, R. R. Vives, A. Magalhaes, *Front. Oncol.* **2021**, *11*, 778752.
[11] a) C. Lanzi, G. Cassinelli, *Biochem. Pharmacol.* **2020**, *178*, 114084; b) R. Lin, S. Xia, C. Shan, D. Chen, Y. Liu, X. Gao, M. Wang, H. B. Kang, Y. Pan, S. Liu, Y. R. Chung, O. Abdel-Wahab, T. Merghoub, M. Rossi, R. R. Kudchadkar, D. H. Lawson, F. R. Khuri, S. Lonial, J. Chen, *Mol. Cell* **2018**, *69*, 923; c) N. Al Matari, G. Deeb, H. Mshiek, A. Sinjab, H. Kadara, W. Abou-Kheir, R. Mhanna, *Molecules* **2020**, *25*, 2595.
[12] N. Zhang, W. Lou, F. Ji, L. Qiu, B. K. Tsang, W. Di, *J. Cancer Res. Clin. Oncol.* **2016**, *142*, 1807.
[13] L. P. Ferreira, V. M. Gaspar, J. F. Mano, *Trends Biotechnol.* **2020**, *38*, 1397.
[14] A. Kusoglu, K. Yangin, S. N. Ozkan, S. Sarica, D. Ornek, N. Solcan, I. C. Karaoglu, S. Kizilel, P. Bulutay, P. Firat, S. Erus, S. Tanju, S. Dilege, E. Ozturk, *ACS Appl. Bio Mater.* **2023**, *6*, 793.
[15] a) E. Ozturk, O. Arlov, S. Aksel, L. Li, D. M. Ornitz, G. Skjak-Braek, M. Zenobi-Wong, *Adv. Funct. Mater.* **2016**, *26*, 3649; b) Ø. Arlov, D. Rütsche, M. Asadi Korayem, E. Öztürk, M. Zenobi-Wong, *Adv. Funct. Mater.* **2021**, *31*, 2010732.
[16] Z. Chen, C. M. Fillmore, P. S. Hammerman, C. F. Kim, K. K. Wong, *Nat. Rev. Cancer* **2014**, *14*, 535.

[17] M. J. Schliekelman, A. Taguchi, J. Zhu, X. Dai, J. Rodriguez, M. Celiktas, Q. Zhang, A. Chin, C. H. Wong, H. Wang, L. McFerrin, S. A. Selamat, C. Yang, E. M. Kroh, K. S. Garg, C. Behrens, A. F. Gazdar, I. A. Laird-Offringa, M. Tewari, Wistuba II, J. P. Thiery, S. M. Hanash, *Cancer Res.* **2015**, *75*, 1789.
[18] M. A. Gillette, S. Satpathy, S. Cao, S. M. Dhanasekaran, S. V. Vasaikar, K. Krug, F. Petralia, Y. Li, W. W. Liang, B. Reva, A. Krek, J. Ji, X. Song, W. Liu, R. Hong, L. Yao, L. Blumenberg, S. R. Savage, M. C. Wendl, B. Wen, K. Li, L. C. Tang, M. A. MacMullan, S. C. Avanessian, M. H. Kane, C. J. Newton, M. Cornwell, R. B. Kothadia, W. Ma, S. Yoo, et al., *Cell* **2020**, *182*, 200.
[19] O. Chaudhuri, S. T. Koshy, C. Branco da Cunha, J. W. Shin, C. S. Verbeke, K. H. Allison, D. J. Mooney, *Nat. Mater.* **2014**, *13*, 970.
[20] A. J. Booth, R. Hadley, A. M. Cornett, A. A. Dreffs, S. A. Matthes, J. L. Tsui, K. Weiss, J. C. Horowitz, V. F. Fiore, T. H. Barker, B. B. Moore, F. J. Martinez, L. E. Niklason, E. S. White, *Am J. Respir. Crit. Care Med.* **2012**, *186*, 866.
[21] A. Barkovskaya, A. Buffone Jr., M. Zidek, V. M. Weaver, *Front. Cell Dev. Biol.* **2020**, *8*, 569377.
[22] K. M. Wisdom, K. Adebowale, J. Chang, J. Y. Lee, S. Nam, R. Desai, N. S. Rossen, M. Rafat, R. B. West, L. Hodgson, O. Chaudhuri, *Nat. Commun.* **2018**, *9*, 4144.
[23] G. T. Gurda, L. Zhang, Y. Wang, L. Chen, S. Geddes, W. C. Cho, F. Askin, E. Gabrielson, Q. K. Li, *Clin. Transl. Med.* **2015**, *4*, e16.
[24] N. Nakamura, E. Miyagi, S. Murata, A. Kawaoi, R. Katoh, *Mod. Pathol.* **2002**, *15*, 1058.
[25] M. Senoo, F. Pinto, C. P. Crum, F. McKeon, *Cell* **2007**, *129*, 523.
[26] D. Cabibi, S. Bellavia, A. G. Giannone, N. Barraco, C. Cipolla, A. Martorana, V. Rodolico, M. Cajozzo, A. M. Florena, *Diagnostics (Basel)* **2020**, *10*, 25.
[27] C. Y. Loh, J. Y. Chai, T. F. Tang, W. F. Wong, G. Sethi, M. K. Shanmugam, P. P. Chong, C. Y. Looi, *Cells* **2019**, *8*, 1118.
[28] J. J. Christiansen, A. K. Rajasekaran, *Cancer Res.* **2006**, *66*, 8319.
[29] D. Kyuno, A. Takasawa, S. Kikuchi, I. Takemasa, M. Osanai, T. Kojima, *Biochim. Biophys. Acta Biomembr.* **2021**, *1863*, 183503.
[30] F. Richardson, G. D. Young, R. Sennello, J. Wolf, G. M. Argast, P. Mercado, A. Davies, D. M. Epstein, B. Wacker, *Anticancer Res.* **2012**, *32*, 537.
[31] Y. Ning, H. Zheng, Y. Zhan, S. Liu, Y. Yang, H. Zang, J. Luo, Q. Wen, S. Fan, J. Exp. Clin. Cancer Res. **2020**, *39*, 162.
[32] S. A. Mani, W. Guo, M. J. Liao, E. N. Eaton, A. Ayyanan, A. Y. Zhou, M. Brooks, F. Reinhard, C. C. Zhang, M. Shipitsin, L. L. Campbell, K. Polyak, C. Brisken, J. Yang, R. A. Weinberg, *Cell* **2008**, *133*, 704.
[33] I. S. Reynolds, M. Fichtner, D. A. McNamara, E. W. Kay, J. H. M. Prehn, J. P. Burke, *Cancer Metastasis Rev.* **2019**, *38*, 237.
[34] D. Vitale, S. Kumar Katakam, B. Greve, B. Jang, E. S. Oh, L. Alaniz, M. Gotte, *FEBS J.* **2019**, *286*, 2870.
[35] D. Nassar, C. Blanpain, *Annu. Rev. Pathol.: Mech. Dis.* **2016**, *11*, 47.
[36] V. Morello, S. Cabodi, S. Sigismund, M. P. Camacho-Leal, D. Repetto, M. Volante, M. Papotti, E. Turco, P. Defilippi, *Oncogene* **2011**, *30*, 4087.
[37] Y. E. Lin, H. D. Long, C. C. Chen, G. C. Liu, F. Li, Y. H. Tian, L. Dai, *J. Thorac. Dis.* **2023**, *15*, 101.
[38] J. Rapp, L. Jaromi, K. Kvell, G. Miskei, J. E. Pongracz, *Respir. Res.* **2017**, *18*, 167.
[39] A. Necchi, D. E. Castellano, B. Mellado, S. Pang, Y. Urun, S. H. Park, U. N. Vaishampayan, G. Currie, E. Abella-Dominicis, S. K. Pal, *J. Clin. Oncol.* **2019**, *37*, 409.
[40] a) C. Gridelli, A. Rossi, D. P. Carbone, J. Guarize, N. Karachaliou, T. Mok, F. Petrella, L. Spaggiari, R. Rosell, *Nat. Rev. Dis. Primers* **2015**, *1*, 15009; b) Y. Pylayeva, K. M. Gillen, W. Gerald, H. E. Beggs, L. F. Reichardt, F. G. Giancotti, *J. Clin. Invest.* **2009**, *119*, 252.
[41] a) A. Dugourd, C. Kuppe, M. Sciacovelli, E. Gjerga, A. Gabor, K. B. Emdal, V. Vieira, D. B. Bekker-Jensen, J. Kranz, E. M. J. Bindels, A. S. H. Costa, A. Sousa, P. Beltrao, M. Rocha, J. V. Olsen, C. Frezza, R. Kramann, J. Saez-Rodriguez, *Mol. Syst. Biol.* **2021**, *17*, e9730; b) N. Tuncbag, S. J. Gosline, A. Kedaigle, A. R. Soltis, A. Gitter, E. Fraenkel, *PLoS Comput. Biol.* **2016**, *12*, e1004879.
[42] D. Masso-Valles, M. E. Beaulieu, L. Soucek, *Expert Opin. Ther. Targets* **2020**, *24*, 101.
[43] A. Carracedo, P. P. Pandolfi, *Oncogene* **2008**, *27*, 5527.
[44] J. Lou, D. J. Mooney, *Nat. Rev. Chem.* **2022**, *6*, 726.
[45] C. Pottier, M. Fresnais, M. Gilon, G. Jerusalem, R. Longuespee, N. E. Sounni, *Cancers* **2020**, *12*, 731.
[46] C. D. Mohan, S. Hari, H. D. Preetham, S. Rangappa, U. Barash, N. Ilan, S. C. Nayak, V. K. Gupta, I. V. Basappa, K. S. Rangappa, *iScience* **2019**, *15*, 360.
[47] a) E. Cerami, J. Gao, U. Dogrusoz, B. E. Gross, S. O. Sumer, B. A. Aksoy, A. Jacobsen, C. J. Byrne, M. L. Heuer, E. Larsson, Y. Antipin, B. Reva, A. P. Goldberg, C. Sander, N. Schultz, *Cancer Discov.* **2012**, *2*, 401; b) J. Gao, B. A. Aksoy, U. Dogrusoz, G. Dresdner, B. Gross, S. O. Sumer, Y. Sun, A. Jacobsen, R. Sinha, E. Larsson, E. Cerami, C. Sander, N. Schultz, *Sci. Signal.* **2013**, *6*, pl1.
[48] A. Naba, K. R. Clauser, S. Hoersch, H. Liu, S. A. Carr, R. O. Hynes, *Mol. Cell. Proteomics* **2012**, *11*, M111014647.
[49] M. Jethalia, S. P. Jani, M. Ceccarelli, R. Mall, *J. Transl. Med.* **2023**, *21*, 558.
[50] a) M. Banda, K. L. McKim, M. B. Myers, M. Inoue, B. L. Parsons, *PLoS One* **2020**, *15*, e0238862; b) K. K. Dijkstra, K. Monkhorst, L. J. Schipper, K. J. Hartemink, E. F. Smit, S. Kaing, R. de Groot, M. C. Wolkers, H. Clevers, E. Cuppen, E. E. Voest, *Cell Rep.* **2020**, *31*, 107588.
[51] A. Dobin, C. A. Davis, F. Schlesinger, J. Drenkow, C. Zaleski, S. Jha, P. Batut, M. Chaisson, T. R. Gingeras, *Bioinformatics* **2013**, *29*, 15.
[52] Y. Liao, G. K. Smyth, W. Shi, *Bioinformatics* **2014**, *30*, 923.
[53] M. I. Love, W. Huber, S. Anders, *Genome Biol.* **2014**, *15*, 550.
[54] Z. Xie, A. Bailey, M. V. Kuleshov, D. J. B. Clarke, J. E. Evangelista, S. L. Jenkins, A. Lachmann, M. L. Wojciechowicz, E. Kropiwnicki, K. M. Jagodnik, M. Jeon, A. Ma'ayan, *Curr. Protoc.* **2021**, *1*, e90.
[55] D. P. Gil, J. N. Law, T. M. Murali, *F1000Res* **2017**, *6*, 58.
[56] P. Shannon, A. Markiel, O. Ozier, N. S. Baliga, J. T. Wang, D. Ramage, N. Amin, B. Schwikowski, T. Ideker, *Genome Res.* **2003**, *13*, 2498.